submitted to *Geophys. J. Int.*

Secular Variation Signals in Magnetic Field Gradient Tensor Elements derived from satellite-based Geomagnetic Virtual Observatories

Magnus D. Hammer, Christopher C. Finlay and Nils Olsen

Division of Geomagnetism, Technical University of Denmark - DTU Space, Kgs. Lyngby, Denmark,

E-mail: magdh@space.dtu.dk

SUMMARY

We present local time series of the magnetic field gradient tensor elements at satellite altitude derived using a Geomagnetic Virtual Observatory (GVO) approach. Gradient element time series are computed in four-monthly bins on an approximately equal-area distributed worldwide network. This enables global investigations of spatial-temporal variations in the gradient tensor elements. Series are derived from data collected by the *Swarm* and CHAMP satellite missions, using vector field measurements and their along-track and East-West differences, when available. We find evidence for a regional Secular Variation impulse (jerk) event in 2017 in the first time derivative of the gradient tensor elements. This event is located at low latitudes in the Pacific region. It has a similar profile and amplitude regardless of the adopted data selection criteria and is well fit by an internal potential field. Spherical harmonic models of the internal magnetic field built from the GVO gradient series show lower noise in near-zonal harmonics compared with models built using standard GVO vector field series. The GVO gradient element series are an effective means of compressing the spatio-temporal information gathered by low-Earth orbit satellites on geomagnetic field variations, which may prove useful for core flow inversions and in geodynamo data assimilation studies.

Key words: Geomagnetism, secular variation, magnetic gradient tensors, *S*warm satellites

1 INTRODUCTION

The main part of the geomagnetic field is generated in the Earth's fluid outer core by a process known as the geodynamo. Knowledge of how this core field varies with space and time provides information on the fluid flow dynamics in the liquid metal outer core. Although the temporal behaviour of the geomagnetic field is well characterized in time series from ground observatories, a global spatial-temporal study is hampered by the uneven distribution of these observatories. Even though low-Earth-orbit (LEO) satellites do provide good global coverage on timescales of weeks and longer, the direct study of the first time derivative of the core field, the secular variation (SV), from satellite measurements is not straightforward as LEO satellites are not geostationary, leading to ambiguity between spatial and temporal variations. Spherical harmonic (SH) field models derived from satellite measurements provide an established way of studying the SV field and its time derivative, the secular acceleration (SA), globally. However, such harmonic functions have global support, which means that a SV prediction at a specific position may be affected by noise from remote locations.

These issues lead Mandea & Olsen (2006) to introduce the concept of Geomagnetic Virtual Observatories (GVOs) in space, in which satellite magnetic measurements from within a selected region, collected during one month time windows, were used to derive a local monthly mean vector field at the satellite mean altitude. The resulting GVO time series resemble monthly mean series computed using ground observatory magnetic measurements, by providing the magnetic vector field elements at fixed locations. However, since they are based on satellite data, regular sampling in both space and time is possible. The GVO method provides a means of compressing satellite data into a manageable dataset with global coverage, together with suitable error estimates. Olsen & Mandea (2007) used CHAMP measurements to derive GVO vector field time series, and carried out a global investigation of SV that identified a regional geomagnetic jerk event in 2003.

In the original GVO approach of Mandea and Olsen, processing of the satellite measurements followed that of simple monthly field means at ground observatories, taking measurements from all local times and with all levels of geomagnetic activity, and relied on the assumption that short period external fields would have zero mean over the course of one month. However, later studies revealed that external fields, especially due to the magnetospheric ring current and ionospheric current systems, cause contamination of the retrieved internal GVO field signal (Olsen & Mandea 2007; Beggan et al. 2009; Domingos et al. 2019). In addition, insufficient local time sampling from within one month of polar orbiting satellites resulted in a bias due to the local time dependence of ionospheric and magnetosphere-ionosphere coupling currents (Shore 2013). Recently, the GVO processing algorithm has been further developed in an effort to reduce contamination from magnetospheric and ionospheric sources, and the local time sampling bias, with the aim of better isolating the field signal generated by the Earth's outer core (Hammer et al. 2021a; Cox et al. 2020). These new GVO vector field series have been used to study global patterns of field changes (Hammer et al. 2021a,c), for inferring fluid flows close to the core surface (Kloss & Finlay 2019; Rogers et al. 2019) and for data assimilation studies (Barrois et al. 2018; Huder et al. 2020).

In parallel to the development of these GVO-based techniques there has also been recent progress in the theory of space-based magnetic gradiometry, inspired by advances in satellite gravimetry. Initial studies have demonstrated that knowledge of the second-order 3×3 magnetic gradient tensor may be beneficial when seeking to retrieve small scale features of the field (both the lithospheric field and the time-dependent core field). This is possible because gradient elements effectively give more weight to shorter wavelengths, while at the same time some noise sources (e.g. unmodeled magnetospheric fields) are predominantly of long wavelength, which can result in a higher signal-to-noise ratio for short wavelengths compared to using the vector field components (Kotsiaros & Olsen 2012, 2014).

Assuming a potential field due to an internal source and no in-situ electrical currents, the field becomes a solenoidal irrotational vector field and the gradient tensor has the special property of being symmetric with a trace of zero. The assumption of a symmetric gradient tensor reduces the number of independent gradient tensor elements from nine to six, while a trace of zero further reduces this number to five. Each element of the magnetic gradient tensor may be considered as a directional filter providing specific information on the magnetic field structures. Thereby, certain gradient tensor elements better constrain specific spherical harmonics (Olsen & Kotsiaros 2011). According to the studies of Kotsiaros & Olsen (2012) and Kotsiaros & Olsen (2014), knowledge of the radial gradient of the radial field, written as $[\nabla B]_{rr}$, is particularly suitable for resolving the higher degree parts and zonal harmonics. The East-West gradient of the azimuthal field, $[\nabla B]_{\phi\phi}$, and radial field, $[\nabla B]_{r\phi}$, are especially sensitive towards sectorial harmonics, while the North-South gradient of the radial, $[\nabla B]_{r\theta}$, and meridional, $[\nabla B]_{\theta\theta}$, fields are especially useful for determining near-zonal harmonics. The East-West gradient of the meridional field, $[\nabla B]_{\theta\phi}$ does not provide significant additional information. In addition, knowledge of how certain external fields may influence certain gradient tensor elements is important to consider, for instance the magnetospheric ring current is expected to affect zonal terms constrained by the $[\nabla B]_{rr}$ element but not the $[\nabla B]_{r\phi}$ element (Kotsiaros & Olsen 2014). Although it is not yet possible to directly measure the full magnetic gradient tensor in space (Nogueira et al.

2015), it is nonetheless possible to compute the tensor elements from a magnetic potential determined using satellite magnetic measurements.

In this paper, we estimate local time series of the magnetic field gradient tensor elements using the GVO method. We follow Hammer et al. (2021a) in implementing dark and quiet time data selection criteria and use 4-month time windows to minimize problems related to local time sampling (Hammer et al. 2021a). In Section 2 we provide a detailed description of the satellite magnetic measurements and selection criteria used, and in Section 3 we describe the GVO method and computation of GVO gradient element time series. In Section 4.1 we present results of the GVO series for each of the SV gradient elements, and visually inspect these. In order to investigate the possible benefits of using GVO gradient data, we compare SH field models derived epoch by epoch from the GVO vector data and GVO gradient tensor data in Section 4.2. We study the detailed behaviour of the gradient tensor elements going from 2015 to 2018 with focus on the Pacific region. Finally, Section 5 provides discussions and conclusions.

2 DATA

To derive the GVO time series we select vector magnetic field measurements from the CHAMP and *Swarm* satellite missions. We used CHAMP L3 magnetic data between July 2000 and September 2010 and *Swarm* Level 1b MAG-L, version 0505/0506, from all three *Swarm* satellites Alpha, Bravo and Charlie between January 2014 and April 2020, and sub-sample at 15s intervals in the vector field magnetometer (VFM) frame. Next, the magnetic data in the VFM frame are rotated into an Earth-Centered Earth-Fixed (ECEF) local Cartesian North-East-Centre (NEC) coordinate frame (for details see Olsen et al. (2006)) by using the Euler rotation angles from the CHAOS-7.2 model (Finlay et al. 2020). Measurements from known problematic days (e.g. where satellite manoeuvres took place) were removed and gross data outliers for which the vector field components deviated more than 500nT from CHAOS-7.2 field model (Finlay et al. 2020) predictions were rejected. The measurements were then selected using a dark quiet time criteria defined here as: a) the sun is at least 10° below horizon, b) geomagnetic activity index $K_p < 3^{\circ}$, c) ring current index $|dRC/dt| < 3\mathrm{nThr}^{-1}$ (Olsen et al. 2014), merging electric field at magnetopause $E_m \leq 0.8\mathrm{mVm}^{-1}$ (Olsen et al. 2014), and placing constraints on the interplanetary magnetic field (IMF) requiring $B_z > 0\mathrm{nT}$ and $|B_y| < 10\mathrm{nT}$ (Ritter et al. 2004). Here we computed two-hourly means of 1 min values of the solar wind and IMF computed form the OMNI database, `http://omniweb.gsfc.nasa.gov`.

Previous studies have demonstrated the benefits of using along-track differences of the satellite magnetic field measurements for retrieving higher spatial resolution of the core and also the lithospheric fields, as such differences filters out correlated noise caused by external sources (Olsen et al.

2015; Kotsiaros et al. 2015; Kotsiaros 2016; Finlay 2019). To facilitate sufficient constraints on the longer wavelengths of the field, we supplement by include data means (Sabaka et al. 2013; Hammer 2018). Therefore, from the satellite magnetic field measurements, $B_k(\mathbf{r})$, where k is the unit vector of a given coordinate system, we use measurement means, Σd_k, and differences, Δd_k as data. The differences, $\Delta d_k = (\Delta d_k^{\text{AT}}, \Delta d_k^{\text{EW}})$, and the means, $\Sigma d_k = (\Sigma d_k^{\text{AT}}, \Sigma d_k^{\text{EW}})$, are taken along-track (AT) for each satellite and East-West (EW) between the *Swarm* Alpha (SWA) and Charlie (SWC) satellites. Here along-track differences are calculated from the 15 s differences $\Delta d_k^{\text{AT}} = [B_k(\mathbf{r}, t) - B_k(\mathbf{r} + \delta\mathbf{r}, t + 15s)]$ while the means are given by $\Sigma d_k^{AT} = [B_k(\mathbf{r}, t) + B_k(\mathbf{r} + \delta\mathbf{r}, t + 15s)]/2$. The East-West differences were calculated as $\Delta d_k^{\text{EW}} = [B_k^{\text{SWA}}(\mathbf{r}_1, t_1) - B_k^{\text{SWC}}(\mathbf{r}_2, t_2)]$, and the means as $\Sigma d_k^{\text{EW}} = [B_k^{\text{SWA}}(\mathbf{r}_1, t_1) + B_k^{\text{SWC}}(\mathbf{r}_2, t_2)]/2$. Considering a given orbit of *Swarm* Alpha, the corresponding *Swarm* Charlie measurement were chosen to be that closest in colatitude provided that $|\Delta t| = |t_1 - t_2| < 50s$ (Olsen et al. 2015).

3 THEORY AND METHOD

3.1 Geomagnetic Virtual Observatory Method

The Geomagnetic Virtual Observatory method allows for epoch estimates of the magnetic vector field components at a given target point (referred to as a GVO target location) to be derived using satellite measurements from within a region closer than 700 km during the course of four months. A radius of 700 km enables enough data for computing reliable and independent GVO estimates every four months (Hammer 2018). From these measurements, provided in an ECEF coordinate frame given by the spherical polar components, $\mathbf{B}^{obs} = (B_r, B_\theta, B_\phi)$, magnetic field residuals are calculated as Hammer et al. (2021a)

$$\delta\mathbf{B} = \mathbf{B}^{obs} - \mathbf{B}^{MF} - \mathbf{B}^{lit} - \mathbf{B}^{mag} - \mathbf{B}^{iono}, \tag{1}$$

where model fields subtracted are: the main field (MF), $\mathbf{B}^{MF}$, for SH degrees $n \in [1, 13]$ determined using the CHAOS-7 model (Finlay et al. 2020), the static lithospheric field, $\mathbf{B}^{lit}$, for SH degrees $n \in [14, 185]$ determined using the LCS-1 model (Olsen et al. 2017), the large-scale magnetospheric and associated Earth induced fields, $\mathbf{B}^{mag}$, as given by the CHAOS-7 model parameterized in time by the RC index (Finlay et al. 2020), and the ionospheric and associated Earth induced fields, $\mathbf{B}^{iono}$, as determined using the CIY4 model parameterized by 90-day averages of solar flux F10.7 (Sabaka et al. 2018). Note here that we remove predictions of the main field in order to facilitate a robust estimation. At a later stage, main field predictions at the GVO target position and epoch are added back (Mandea

& Olsen 2006; Hammer et al. 2021a), however, the precise choice of main field used in both steps is not crucial (Hammer 2018; Hammer et al. 2021c).

Next, the residual magnetic field vector, eq.(1), and its positions are transformed from the spherical system to a right-handed local topocentric Cartesian system (x, y, z) having its origin at the GVO target location, as detailed in (Hammer 2018, p. 64). At this specific GVO location (and only at this location), x points towards geographic south, y points towards east and z points radially upwards (Hammer et al. 2021a). At the GVO target point, the unit vectors of the local Cartesian frame, $(\hat{\mathbf{e}}_\mathbf{x}, \hat{\mathbf{e}}_\mathbf{y}, \hat{\mathbf{e}}_\mathbf{z})$, also coincides with the spherical polar unit vectors $(\hat{\mathbf{e}}_\mathbf{r}, \hat{\mathbf{e}}_\theta, \hat{\mathbf{e}}_\phi)$. Assuming that the magnetic field measurements are made in a source free region, the residual field, $\delta\mathbf{B}$, is a Laplacian potential field which fulfils the quasi-stationary approximation (Sabaka et al. 2010). This means that a magnetic scalar potential, V, is associated with the residual field, which in the local Cartesian coordinate system can be expanded as a sum of polynomials having the form $C_{abc}x^a y^b z^c$ (Backus et al. 1996). In this application we expand to cubic terms following Hammer et al. (2021a)

$$
\begin{aligned}
V(x, y, z) &= C_{100}x + C_{010}y + C_{001}z + C_{200}x^2 + C_{020}y^2 \\
&- (C_{200} + C_{020})z^2 + C_{110}xy + C_{101}xz + C_{011}yz \\
&- \frac{1}{3}(C_{102} + C_{120})x^3 - \frac{1}{3}(C_{210} + C_{012})y^3 \\
&- \frac{1}{3}(C_{201} + C_{021})z^3 + C_{210}x^2y + C_{201}x^2z \\
&+ C_{120}y^2x + C_{021}y^2z + C_{102}z^2x + C_{012}z^2y + C_{111}xyz. \qquad (2)
\end{aligned}
$$

The means and differences of the residual magnetic field are linked to this potential via appropriate design matrices constructed as described in Hammer et al. (2021a). The coefficients of the potential are determined from a robust least-squares solution, which includes a) an a prior data covariance matrix derived from standard deviations of the residuals between the data (means and differences) and predictions of an un-weighted least-squares solution, b) a diagonal weight matrix consisting of robust (Huber) weights, using a scale constant of 1.5 (e.g., Constable 1988), and c) an additional down-weighting factor of 1/2 when data comes from *Swarm* satellites Alpha and Charlie, taking into account that these fly side-by-side and thus provide similar measurements. From these potential coefficients, a mean residual magnetic field for the given GVO target point position and epoch is computed as $\delta\mathbf{B}_{GVO}(x, y, z) = -\nabla V = -(C_{100}, C_{010}, C_{001})$. This mean residual field is then rotated back into the vector components in spherical polar coordinates, $\delta B_{GVO,r} = \delta B_{GVO,z}$, $\delta B_{GVO,\theta} = \delta B_{GVO,x}$, $\delta B_{GVO,\phi} = \delta B_{GVO,y}$ and afterwards a main field prediction evaluated at the GVO epoch using SH degrees $n \in [1, 13]$ is added back to obtain the GVO field (Hammer et al. 2021a).

Following the same procedure as in Hammer et al. (2021a), we compute a global grid of 300

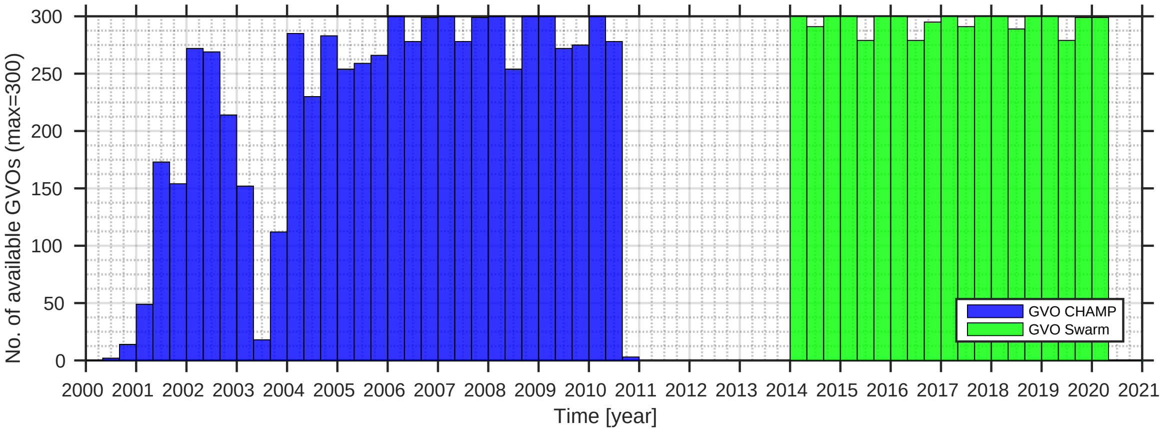

Figure 1. Number of stable GVOs for each epoch, given the applied dark and quiet-time selection criteria, during CHAMP (blue) and *Swarm* (green) times.

GVO's located on an approximately equal area grid based on the sphere partitioning algorithm of Leopardi (2006). The distance between the GVOs in this grid is $\approx 1400\,\mathrm{km}$, and with a target cylinder radius of 700 km close to 80% of the measurements are used. The GVO height above ground is taken to be 370 km and 490 km (approximate mean orbital altitude) during CHAMP and *Swarm* times, respectively. The global grid has GVOs located at the North and South poles, where we define the (r, θ, ϕ) frame such that r points radially outwards, θ is aligned along the Greenwich meridian and ϕ completes the right-handed system. In order to add back a main field prediction at these two positions, we compute an average value of model field predictions computed 0.1° in latitude from the North/South Pole at longitudes 0° and 180°. Figure 1 presents the available number of GVOs for each epoch (the maximum possible number at each epoch is 300). Table 1 presents the mean and root-mean-square (rms) of residuals between the satellite measurements used for each GVO and the GVO model predictions, and summed up for each component split into regions of 78 polar and 222 non-polar GVO's, defining polar to be GVOs poleward of $\pm 54^\circ$ geographic latitude. The polar rms values for both data sums and differences are higher than the non-polar, and the CHAMP values are higher than the *Swarm* values. The non-polar rms values for all components are below 2nT during both CHAMP and *Swarm* times.

3.2 Computing the Magnetic Field Gradient Tensor within the GVO framework

In this section we now proceed to formulate the magnetic field gradient tensor and describe how this transforms from a spherical polar coordinate system to the local topocentric Cartesian right-handed coordinate system used in the GVO method. This transformation will allow us to compute GVO time series for the magnetic field gradient tensor elements in analogy to the concept of GVO vector field time series.

	CHAMP			Swarm				CHAMP			Swarm		
Component	No.	Mean [nT]	rms [nT]	No.	Mean [nT]	rms [nT]	Component	No.	Mean [nT]	rms [nT]	No.	Mean [nT]	rms [nT]
Polar	2574			1638			**Non-polar**	7326			4662		
$\sum B_{x,NS}$		-0.30	6.61		-0.52	6.26	$\sum B_{x,NS}$		-0.80	1.75		0.01	1.69
$\sum B_{y,NS}$		0.00	6.52		-0.02	6.79	$\sum B_{y,NS}$		0.00	1.46		0.00	1.74
$\sum B_{z,NS}$		0.00	3.33		0.01	3.02	$\sum B_{z,NS}$		0.00	1.30		-0.00	0.95
$\sum B_{x,EW}$					0.05	5.92	$\sum B_{x,EW}$					-0.03	1.57
$\sum B_{y,EW}$					-0.01	6.44	$\sum B_{y,EW}$					0.01	1.48
$\sum B_{z,EW}$					0.01	2.89	$\sum B_{z,EW}$					-0.01	0.88
$\Delta B_{x,NS}$		-0.01	4.35		0.01	3.80	$\Delta B_{x,NS}$		-0.01	0.50		0.00	0.26
$\Delta B_{y,NS}$		-0.01	5.20		-0.01	4.86	$\Delta B_{y,NS}$		0.00	0.58		0.00	0.38
$\Delta B_{z,NS}$		0.01	1.61		-0.00	1.36	$\Delta B_{z,NS}$		0.00	0.53		0.00	0.27
$\Delta B_{x,EW}$					0.10	3.17	$\Delta B_{x,EW}$					0.10	0.51
$\Delta B_{y,EW}$					0.00	3.17	$\Delta B_{y,EW}$					0.02	0.70
$\Delta B_{z,EW}$					-0.07	0.95	$\Delta B_{z,EW}$					-0.02	0.50

Table 1. GVO model rms misfit statistics between contributing satellite data and GVO estimates using a global grid of 300 GVO's during CHAMP and *Swarm*. Here $\sum$ and Δ represent data means and data differences, respectively.

We begin by expressing the magnetic field gradient tensor in the local Cartesian system of the GVO method described in Section 3.1. This is given by (see Appendix A for full details)

$$\nabla \mathbf{B} = -\begin{pmatrix} \frac{\partial^2 V}{\partial z^2} & \frac{\partial^2 V}{\partial x \partial z} & \frac{\partial^2 V}{\partial y \partial z} \\ \frac{\partial^2 V}{\partial z \partial x} & \frac{\partial^2 V}{\partial x^2} & \frac{\partial^2 V}{\partial y \partial x} \\ \frac{\partial^2 V}{\partial z \partial y} & \frac{\partial^2 V}{\partial x \partial y} & \frac{\partial^2 V}{\partial y^2} \end{pmatrix} = \begin{pmatrix} [\nabla B]_{zz} & [\nabla B]_{zx} & [\nabla B]_{zy} \\ [\nabla B]_{xz} & [\nabla B]_{xx} & [\nabla B]_{xy} \\ [\nabla B]_{yz} & [\nabla B]_{yx} & [\nabla B]_{yy} \end{pmatrix}. \tag{3}$$

This is a second-order tensor where the minus sign comes from defining the magnetic field as the negative gradient of the potential. The gradient tensor elements are denoted here by $[\nabla B]_{jk}$, where the first subscript, j denotes the vector component under consideration and the second subscript, k, denotes direction of the field derivative. Using the local cubic potential eq.(2) estimated from the residual magnetic field as described in Section 3.1, a second-order residual field gradient tensor at the GVO target point can be derived using eq.(3) as

$$\nabla \delta \mathbf{B}_{GVO} = \begin{pmatrix} 2(C_{200} + C_{020}) & -2C_{101} & -2C_{011} \\ -2C_{101} & -2C_{200} & -2C_{110} \\ -2C_{011} & -2C_{110} & -2C_{020} \end{pmatrix}. \tag{4}$$

Because the magnetic field is a solenoidal vector field, the divergence is zero, such that the trace of the gradient tensor vanishes, i.e. $tr(\nabla\delta\mathbf{B}_{GVO}) = 2(C_{200} + C_{020}) - 2C_{200} - 2C_{020} = 0$, reducing the number of independent elements from 9 to 8. In addition to this, because the field is a Laplacian potential field, the curl of the field vanishes and the number of independent tensor elements reduces to 5; in other words, the magnetic gradient tensor is symmetric with trace zero (Kotsiaros & Olsen 2012).

Following the GVO algorithm, gradient tensor estimates from a field model then have to be added back at the GVO target point for harmonic degrees $n \leq 13$. To do this, we will need to consider how the gradient tensor elements in spherical polar and Cartesian coordinate systems are related. The magnetic gradient tensor elements as expressed in the spherical coordinate system are given by (Olsen & Kotsiaros 2011; Kotsiaros & Olsen 2012), see also Appendix A

$$\nabla\mathbf{B} = \begin{pmatrix} -\frac{\partial^2 V}{\partial r^2} & -\frac{1}{r}\frac{\partial^2 \partial V}{\partial\theta\partial r} + \frac{1}{r^2}\frac{\partial V}{\partial\theta} & -\frac{1}{r\mathrm{sin}\theta}\frac{\partial^2 V}{\partial\phi\partial r} + \frac{1}{r^2\mathrm{sin}\theta}\frac{\partial V}{\partial\phi} \\ -\frac{\partial^2 V}{\partial r\partial\theta} + \frac{1}{r^2}\frac{\partial V}{\partial\theta} & -\frac{1}{r^2}\frac{\partial^2 V}{\partial\theta^2} - \frac{1}{r}\frac{\partial V}{\partial r} & -\frac{1}{r^2\mathrm{sin}\theta}\frac{\partial^2 V}{\partial\phi\partial\theta} + \frac{\mathrm{cos}\theta}{r^2\mathrm{sin}^2\theta}\frac{\partial V}{\partial\phi} \\ -\frac{1}{r\mathrm{sin}\theta}\frac{\partial^2 V}{\partial r\partial\phi} + \frac{1}{r^2\mathrm{sin}\theta}\frac{\partial V}{\partial\phi} & -\frac{1}{r^2\mathrm{sin}\theta}\frac{\partial^2 V}{\partial\theta\partial\phi} + \frac{\mathrm{cos}\theta}{r^2\mathrm{sin}^2\theta}\frac{\partial V}{\partial\phi} & -\frac{1}{r^2\mathrm{sin}^2\theta}\frac{\partial^2 V}{\partial\phi^2} - \frac{1}{r}\frac{\partial V}{\partial r} - \frac{\mathrm{cos}\theta}{r^2\mathrm{sin}^2\theta}\frac{\partial V}{\partial\theta} \end{pmatrix}$$

$$= \begin{pmatrix} [\nabla B]_{rr} & [\nabla B]_{r\theta} & [\nabla B]_{r\phi} \\ [\nabla B]_{\theta r} & [\nabla B]_{\theta\theta} & [\nabla B]_{\theta\phi} \\ [\nabla B]_{\phi r} & [\nabla B]_{\phi\theta} & [\nabla B]_{\phi\phi} \end{pmatrix}. \tag{5}$$

Here the first column of the tensor contains the derivatives of the magnetic field components along the radial direction, the second column contains the derivatives along the co-latitudinal direction and the third column contains the derivatives along the longitudinal direction. The gradient element in the first column and row contains one term only, the field derivative term e.g. $\partial^2/\partial r^2$, while the rest of the gradient tensor elements in addition to this also have an additional field term i.e. $\partial/\partial r$, $\partial/\partial\theta$ or $\partial/\partial\phi$. Appendix B provides example plots of the SV gradient tensor elements at the Earth's surface in 2018, decomposed into the field derivative term, the field term parts and both terms together as computed using the CHAOS-7 field model (Finlay et al. 2020). The transformations relating the gradient tensor elements in the local Cartesian system to the tensor elements of the spherical system, *only at the GVO target location*, are in the end given by the following simple relations (see Appendix A for a full derivation).

$$\begin{aligned} [\nabla B]_{zz} &= [\nabla B]_{rr} & [\nabla B]_{zx} &= [\nabla B]_{r\theta} & [\nabla B]_{zy} &= [\nabla B]_{r\phi} \\ [\nabla B]_{xz} &= [\nabla B]_{\theta r} & [\nabla B]_{xx} &= [\nabla B]_{\theta\theta} & [\nabla B]_{xy} &= [\nabla B]_{\theta\phi} \\ [\nabla B]_{yz} &= [\nabla B]_{\phi r} & [\nabla B]_{yx} &= [\nabla B]_{\phi\theta} & [\nabla B]_{yy} &= [\nabla B]_{\phi\phi}\,. \end{aligned} \tag{6}$$

Having determined the potential from the residual magnetic field eq.(1), we can compute a residual

Component	$rms_{[rr]}$ $[pT/km\,yr^{-1}]$	$rms_{[\theta\theta]}$ $[pT/km\,yr^{-1}]$	$rms_{[\phi\phi]}$ $[pT/km\,yr^{-1}]$	$rms_{[r\theta]}$ $[pT/km\,yr^{-1}]$	$rms_{[r\phi]}$ $[pT/km\,yr^{-1}]$	$rms_{[\theta\phi]}$ $[pT/km\,yr^{-1}]$
CHAMP						
Polar	5.40	3.90	4.20	4.20	5.20	5.20
non-Polar	2.10	0.70	2.00	1.40	3.20	1.30
All	2.98	1.54	2.55	2.14	3.73	2.33
Swarm						
Polar	4.20	3.20	3.80	3.20	3.40	4.30
non-Polar	1.20	0.30	1.20	0.50	1.50	1.10
All	1.98	1.01	1.86	1.23	1.97	1.97

Table 2. Mean of the rms differences (in $\mathrm{pT/km\,yr^{-1}}$) between GVO SV series and GCV cubic spline fits for six of the gradient tensor elements. Results are shown for GVO SV gradient series derived from *Swarm* and CHAMP data using CHAOS-7.2 (Finlay et al. 2020) as MF model in the GVO processing.

field gradient tensor by eq.(4) and add back main field gradient tensor estimates from the CHAOS-7.2 field model using eq.(5) for SH degrees $n \leq 13$, using the above relations, in order to obtain the required GVO field gradient estimates $\nabla\mathbf{B}_{GVO}$. Note that this procedure is analogous to the procedure applied in deriving vector field GVOs where the main vector field is added back. The above procedure is then repeated at each GVO location and for each epoch to compute all the desired GVO field gradient time series.

Error estimates for each tensor element jk, and separately for CHAMP and *Swarm*, are computed using the residuals $e_{jk} = d^{GVO} - d^{CHAOS}$, between the GVO gradient tensor data, $d^{GVO} = [\nabla B_{GVO}]_{jk}$, and the gradient element predictions of the CHAOS-7 for SH degree $n = 1 - 16$, $d^{CHAOS} = [\nabla B]_{jk}$. Considering all epochs for each GVO in the grid, the error estimates for tensor element jk are given by the total mean square error $\sigma_{jk} = \sqrt{\sum_i (e_{jk,i} - \mu_{jk})^2/M + \mu_{jk}^2}$ (e.g. Bendat & Piersol 2010), where $e_{jk,i}$ is the residual of the ith data element, M is the number of data in a given series and μ_{jk} is the residual mean for a given component. Hammer et al. (2021a) computed similar uncertainty estimates for the vector components using the vector field residuals towards the CHAOS-7 model.

As with the ordinary GVO vector field time series, we estimate GVO gradient tensor time series in a global grid of 300 GVOs. We compute the SV as annual differences at each GVO for each tensor element. In order to quantify the scatter levels in each series, we then fit cubic smoothing splines to the time series, with a knot spacing of 4 months and a smoothing parameter determined using a generalized cross-validation (GCV) approach (Green & Silverman 1993). Table 2 presents

Component	$rms_{[rr]}$ $[pT/km\,yr^{-1}]$	$rms_{[\theta\theta]}$ $[pT/km\,yr^{-1}]$	$rms_{[\phi\phi]}$ $[pT/km\,yr^{-1}]$	$rms_{[r\theta]}$ $[pT/km\,yr^{-1}]$	$rms_{[r\phi]}$ $[pT/km\,yr^{-1}]$	$rms_{[\theta\phi]}$ $[pT/km\,yr^{-1}]$
CHAMP						
Polar	5.40	3.90	4.20	4.20	5.20	5.20
non-Polar	2.10	0.70	2.00	1.40	3.20	1.30
All	2.98	1.55	2.55	2.14	3.72	2.33
Swarm						
Polar	4.20	3.20	3.80	3.20	3.40	4.30
non-Polar	1.20	0.30	1.20	0.50	1.40	1.20
All	1.97	1.02	1.86	1.22	1.97	1.97

Table 3. Mean of the rms differences (in $\mathrm{pT/km\,yr^{-1}}$) between GVO SV series and GCV cubic spline fits for six of the gradient tensor elements. Results are shown for GVO SV gradient data derived from *Swarm* and CHAMP data using COV-OBS.x2 model (Huder et al. 2020) as MF model in the GVO processing.

the mean rms differences between the GVO SV gradient tensor elements and GCV spline fits, separated into polar and non-polar regions. These rms numbers provide an indication of the scatter level in the GVO SV gradient data derived from the CHAMP and *Swarm* measurements first using CHAOS-7 (Finlay et al. 2020) as a main field model. Comparing the numbers between CHAMP and *Swarm*, we see that overall the values are lower for *Swarm*, i.e. *Swarm* gradient tensor element SV time series have a lower scatter than similar series for CHAMP. In particular, we note that the $d\,[\nabla B]_{\theta\theta}\,/dt$ and $d\,[\nabla B]_{r\theta}\,/dt$ elements show considerably lower misfit values having non-polar values of $0.3\ \mathrm{pT/km\,yr^{-1}}$ and $0.5\ \mathrm{pT/km\,yr^{-1}}$, respectively, during *Swarm* and $0.7\ \mathrm{pT/km\,yr^{-1}}$ and $1.4\ \mathrm{pT/km\,yr^{-1}}$ during CHAMP times, respectively.

We also tested how the choice of main field model (used for subtracting and adding back main field estimates) would impact the results. We produced test GVO tensor element series from both CHAMP and *Swarm* measurements using the main field predictions for SH degrees $n \in [1, 13]$ of the COV-OBS.x2 model (Huder et al. 2020). Table 3 presents the mean rms differences using the COV-OBS.x2 model instead of CHAOS-7. This results in almost identical misfit levels to the GCV splines (i.e. scatter), between the GVO gradient series during CHAMP and *Swarm* times, regardless of whether CHAOS-7.2 or COV-OBS.x2 is chosen.

4 RESULTS

4.1 Field Gradient Element SV time series

We begin by investigating the temporal behaviour of the annual differences of each gradient tensor element at an example GVO location above Honolulu ground observatory in Hawaii, from which there are well known vector field records. To do this, we compute dedicated GVO gradient element series above the Honolulu observatory using the method described in Section 3.2. Here we are motivated by studies which have point out a change in secular acceleration of the radial component in the Pacific occurring around 2017 (Sabaka et al. 2018; Finlay et al. 2020). In particular, we are interested to see if it is possible to identify this event in the GVO gradient tensor time series, and how this will display in the various tensor elements. Figure 2 present plots of the SV for each gradient tensor element above Honolulu, showing the GVOs derived from CHAMP (in blue) and *Swarm* (in red) measurements. For comparison purposes we have mapped the two GVO series to a common altitude of 500 km by subtracting off the SV gradient field differences between the GVO altitudes and 500 km altitude using the CHAOS-7.2 model.

We begin by noting that the SV gradient tensor in Figure 2 is symmetric, as expected. Visual inspection clearly demonstrates that geophysical signals are captured in all of the SV gradient tensor elements. Distinctive changes centred around 2017 can be observed having a "V" shape in the $d\left[\nabla B\right]_{rr}/dt$ and $d\left[\nabla B\right]_{r\theta}/dt$ elements, with a corresponding "Λ" shape in the $d\left[\nabla B\right]_{\theta\theta}/dt$ and $d\left[\nabla B\right]_{\phi\phi}/dt$ elements. In addition to this, we note that during 2004-2010, especially the $d\left[\nabla B\right]_{r\theta}/dt$ element displays a variation pattern which resembles that found in the θ-component of the annual differences of monthly mean vector field series from Honolulu (not shown).

Next, we investigate the global behaviour of annual differences of the gradient elements for GVOs derived from *Swarm* measurements during 2014-2020. Here we have chosen to present global series for the $d\left[\nabla B\right]_{rr}/dt$ element in Figure 3. By visual inspection, we find local regions with similar temporal changes as those observed at the Honolulu SV gradient series. In particular, a distinct "V" shaped behaviour is found in the eastern Pacific region in a band stretching from latitudes 20°S to 20°N and longitudes $180°$ to $220°$ with a possibly related opposite "Λ" shaped behaviour in the western Pacific region from latitudes $20°$S to $20°$N and longitudes $120°$E to $180°$E. These regional changes occur over a time window of 6 years reaching amplitudes of about $15\,\mathrm{pT/km\,yr^{-1}}$. Note that a "$V$"-shaped SV gradient time series means a strong positive change in the SA, while a "Λ"-shaped time series means a strong negative change in the SA. Though more complex to interpret, the other SV gradient tensor elements (not shown) also exhibit distinctive behaviour in the Pacific region. These observed changes in the SV gradient elements indicate regional jerk-type event happening in the Pacific centred

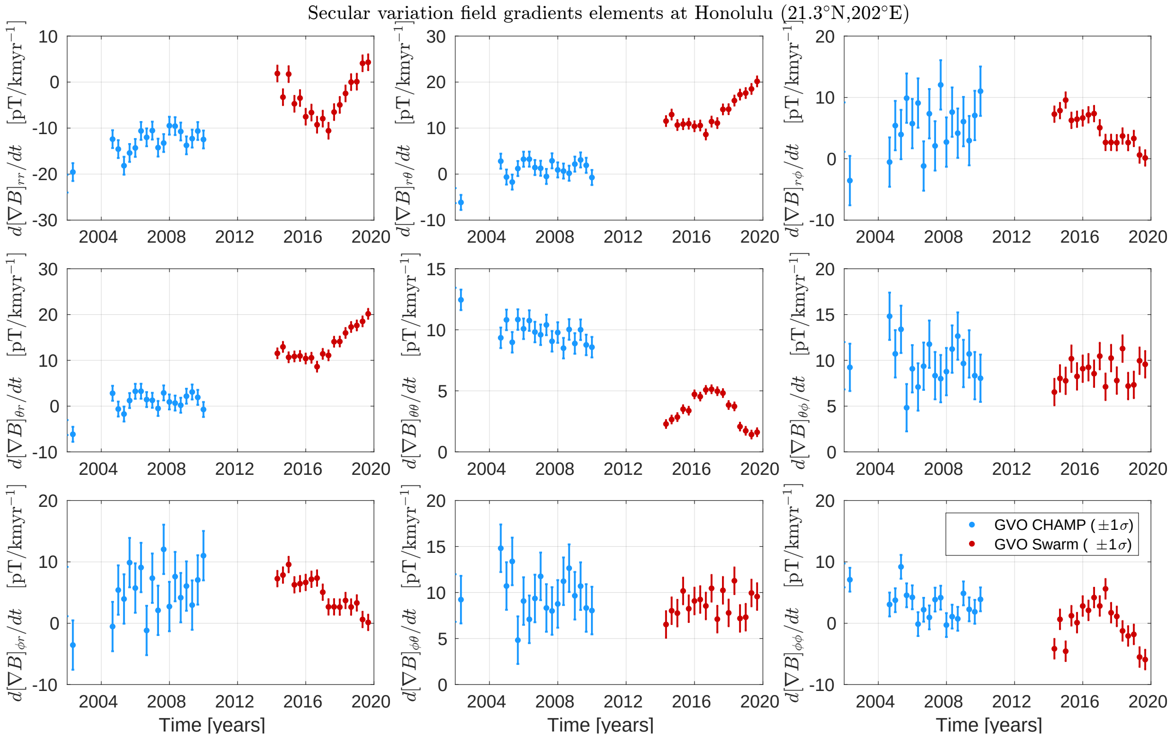

Figure 2. Annual differences of the GVO field gradient elements with $\pm1\sigma$ uncertainties, during CHAMP (blue) and *Swarm* (red) times at altitude 500km for a case study above Honolulu, Hawaii. Units are $\mathrm{pT/km\,yr^{-1}}$.

on 2017. In the ionosphere external fields tend to be organized according to the geometry of Earth's main field, and their signal in the GVO series may therefore be grouped accordingly to magnetic latitude in quasi-dipole coordinates (Laundal & Richmond 2017). Here magnetic latitude $\pm70°$ (dark blue curve) may be used to approximate the border between North/South Polar and Auroral zones, while magnetic latitude $\pm50°$ (light blue curve) divides the North/South Auroral and Low- to Mid-latitude zones (Hammer et al. 2021a). In all of the SV gradient element maps, higher scatter are found at GVOs located in the Polar and Auroral zones, which is consistent with noise (unmodeled fields) from ionospheric and magnetosphere-ionosphere coupling currents.

Besides the aforementioned variations, rapid small amplitude SV fluctuations within a few years can be seen especially clear in the $d\,[\nabla B]_{rr}\,/dt$ element. Are such rapid changes of external origin? In particular, two types of variations in the SV gradient series could be indicative of external field leakage: 1) a temporal feature seen in polar latitude GVO time series persisting in series at lower latitudes along the same meridional line, could be an indicator of a contaminating signal of ionospheric or field-aligned current origin, due to the incomplete sampling of local times in the contributing satellite data 2) temporal features seen at mid or low latitudes in the GVO series at all longitudes could be a sign of a signal having magnetospheric origin. In the global time series no distinct similar temporal feature

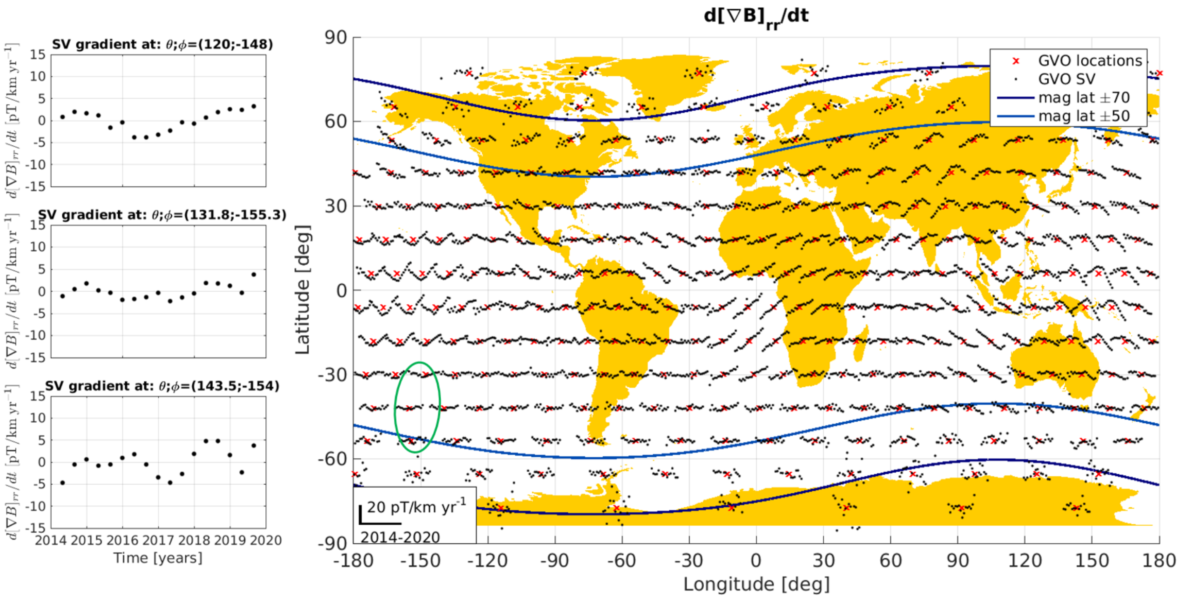

Figure 3. Time series of SV field gradient element $d\,[\nabla B]_{rr}\,/dt$ (map) during *Swarm* time from 2014-2020 at 490km altitude. Magnetic latitudes $\pm 50°$ and $\pm 70°$ shown with blue curves. GVO locations marked with a red cross. Highlighted are selected time series (locations marked with green ellipse) after removing the mean trend in order to ease comparison, at three GVO locations along the $150°$W meridian line at latitudes $30°$S (top), $42°$S (center) and $54°$S (bottom).

can be observed along all longitudes at mid/low latitudes, thus suggesting that magnetospheric disturbances are small. However, some contamination from ionospheric currents at higher latitudes persists to lower latitudes. Considering for instance $d\,[\nabla B]_{rr}\,/dt$ series along longitude $150°$W, stretching from latitudes $30°$S to $60°$S, some rapid variations can be seen that decrease in amplitude going towards equatorial latitudes, as highlighted in the side-panels of Figure 3 at three selected GVO locations (marked in the global maps by the green ellipse).

An important question is whether the prominent change in SV observed centred on 2017 is robust and of internal origin. To address this, we produced a set of the GVO SV series above Honolulu, during *Swarm* time, testing a range of geomagnetic selection criteria. We considered five cases: Case A using a dark quiet time data selection removing estimates of the magnetospheric and ionospheric fields as described in Section 2, this is our ’preferred’ criteria for studying core field variations, Case B using a dark quiet time data selection removing estimates of the magnetospheric field but not removing estimates of the ionospheric field, Case C using a dark time data selection but with neither ionospheric nor magnetospheric corrections, Case D using a quiet time data selection from both day and night (”all” local times) and estimates of the magnetospheric field were removed and Case E using data from ”all” local times, without any quiet time data selection applied and without corrections for magnetospheric or ionospheric fields. Here ”dark” means the sun is required to be at least $10°$ below horizon, and ”all”

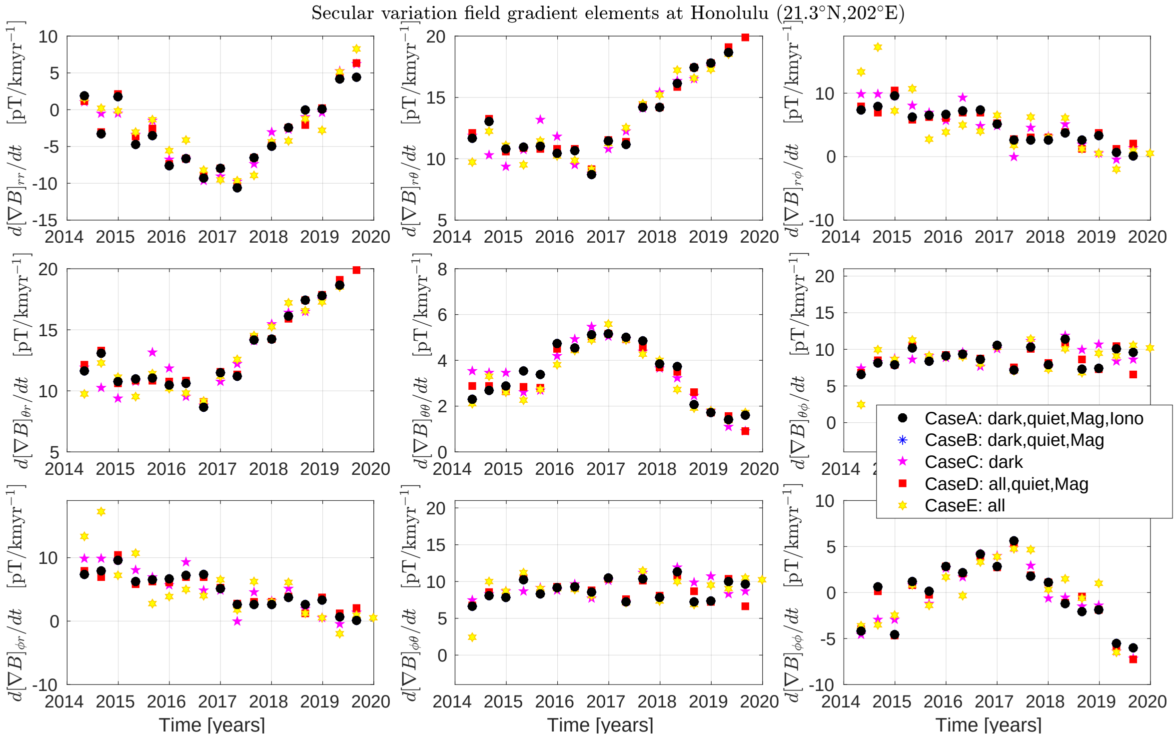

Figure 4. Annual differences of the field gradient elements from GVO's derived using different data selection criteria, as described in the text, during *Swarm* time for a case study at Honolulu, Hawaii. Units are $\mathrm{pT/km\,yr^{-1}}$.

means that no such requirement is used, i.e. sunlit data are also included. SV gradient series for all five data selection cases are shown in Figure 4. The black dots corresponding to Case A are for our "preferred" criteria were also used to derive the maps in Figure 3. All the selection criteria results in the same overall temporal "Λ/V" shape behaviour with an amplitude of $\approx 15\ \mathrm{pT/km\,yr^{-1}}$. There is no increase in amplitude on including more disturbed data. For example, comparing Case C (purple star) with Case A/Case B (black/blue dots) should expose a signal from a magnetospheric source; however, the same "Λ/V" shape behaviour appears in all three cases. Comparing instead Case E (yellow star) with Case C and Case D should expose an ionospheric signal, which is expected to be larger during sunlit conditions; even though more scatter is seen in Case E, the same overall "Λ/V" shape is clearly visible and with similar amplitude. These results are consistent with an internal origin for the 2017 SV impulse event.

4.2 Example Spherical Harmonic Models Derived From Gradient Data

In this section we demonstrate that spherical harmonic (SH) field models with high temporal resolution (4 months) can be built from the global network of GVO gradient tensor time series. We then use these models to investigate global change in SA during *Swarm* time, and in particular, we analyse the possible benefits of the GVO field gradient tensor series over more standard GVO vector field series. The linear forward problem of determining the SH expansion coefficients can be written

$$\mathbf{d} = \underline{\underline{\mathbf{G}}}\mathbf{m}, \tag{7}$$

where $\mathbf{d}$ is a data vector containing the GVO epoch data (i.e. field vector components or field gradient tensor elements), $\underline{\underline{\mathbf{G}}}$ is the design matrix for an internal potential relating each model coefficient to the data, and vector $\mathbf{m}$ contains the parameters of the potential, i.e. the internal SH coefficients here denoted as g_n^m and h_n^m for order m and degree n. For each GVO epoch we estimate a SH model using a robust least-squares solution

$$\mathbf{m} = (\underline{\underline{\mathbf{G}}}^T \underline{\underline{\mathbf{W}}}\, \underline{\underline{\mathbf{G}}})^{-1} \underline{\underline{\mathbf{G}}}^T\, \underline{\underline{\mathbf{W}}}\mathbf{d}, \tag{8}$$

where $\underline{\underline{\mathbf{W}}} = w/\sigma^2$ is a diagonal weighting matrix consisting of Huber weights, w, having a Huber tuning of 1.5 (e.g., Constable 1988) and error estimates, σ^2, of either the field vector components or field gradient tensor elements (see Section 3.2). We derive models up to SH degree 14 for each 4 month interval. No spatial or temporal regularization is applied.

To investigate the 2017 region jerk event we next compute the secular acceleration change for each gradient tensor element between 2015.5 and 2018.5 at the Earth's surface

$$\Delta d^2 \left[\nabla B\right]_{jk} / dt^2 = d^2 \left[\nabla B\right]_{jk} / dt^2|_{2018.5} - d^2 \left[\nabla B\right]_{jk} / dt^2|_{2015.5}. \tag{9}$$

Plotting global maps of this change in Figure 5 for each of the gradient elements for degrees $n \leq 9$ at the Earth's surface, distinct patterns of SA change are seen to have occurred in the Pacific region during 2015.5-2018.5. Only results for the upper right part of the gradient elements are shown as the tensor is symmetric. The $\Delta d^2 \left[\nabla B\right]_{rr} / dt^2$ map identifies two strong localized patches of opposite sign in SA change reaching amplitudes of $40\ \mathrm{pT/km\,yr^{-2}}$ in a region defined by latitudes $25°$S to $25°$N and longitudes $140°$ to $220°$. Associated strong negative and positive patches are seen in the $\Delta d^2 \left[\nabla B\right]_{\phi\phi} / dt^2$ map in the same region. In addition, the $\Delta d^2 \left[\nabla B\right]_{r\theta} / dt^2$ and $\Delta d^2 \left[\nabla B\right]_{\theta\phi} / dt^2$ elements show a tiling pattern of positive and negative field patches from latitudes $25°$S to $25°$N and longitudes $120°$ to $240°$. Similar changes, but in the radial field SA between 2014 to 2020, involving nearby features with opposite sign in the Pacific region, have been found in the CHAOS-7 field model (Finlay et al. 2020) and using the technique of Subtractive Optimized Local Averages (SOLA) applied to *Swarm* data (Hammer & Finlay 2019; Hammer et al. 2021c).

Next, we seek to further inspect and compare the SH models obtained from GVO the field gradient series with similar models obtained using more traditional GVO vector field series. Figure 6 presents the mean of the MF (dotted curves), SV (solid curves) and SA (punctuated curves) power spectra at the CMB obtained from the epoch-by-epoch SH models derived without applying any spatial or

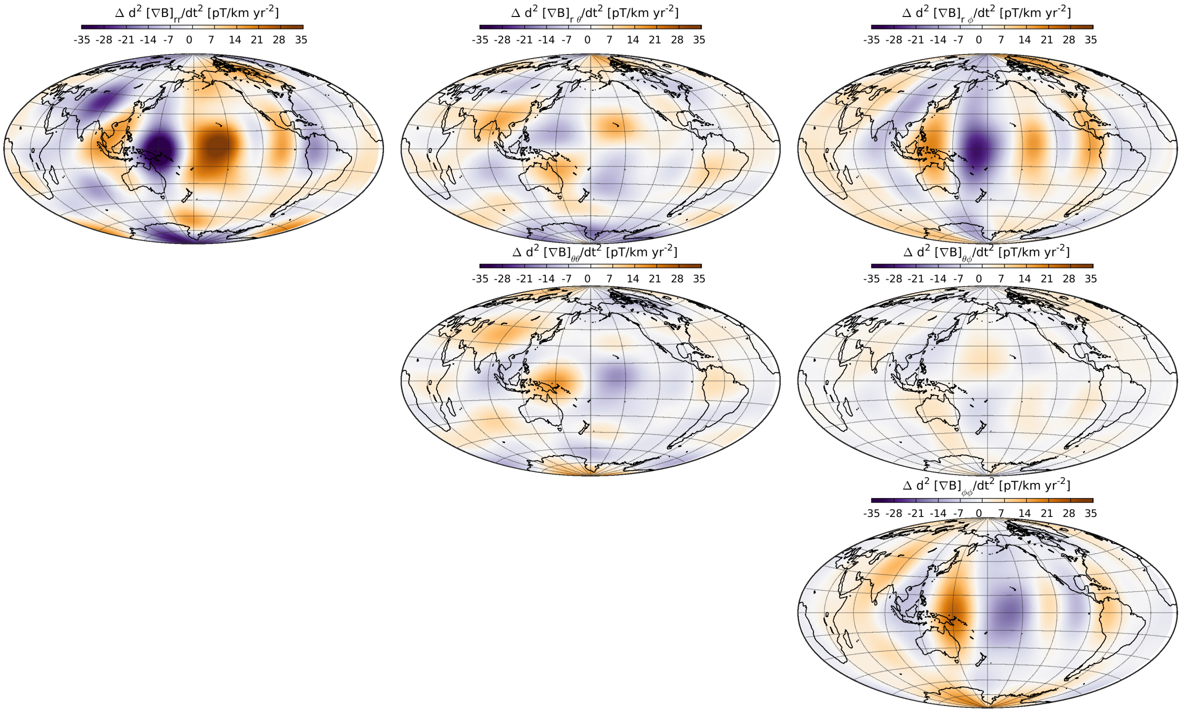

Figure 5. Change in SA gradient tensor elements between 2015.5 and 2018.5 for SH degrees $n \leq 9$ at the Earth's surface.

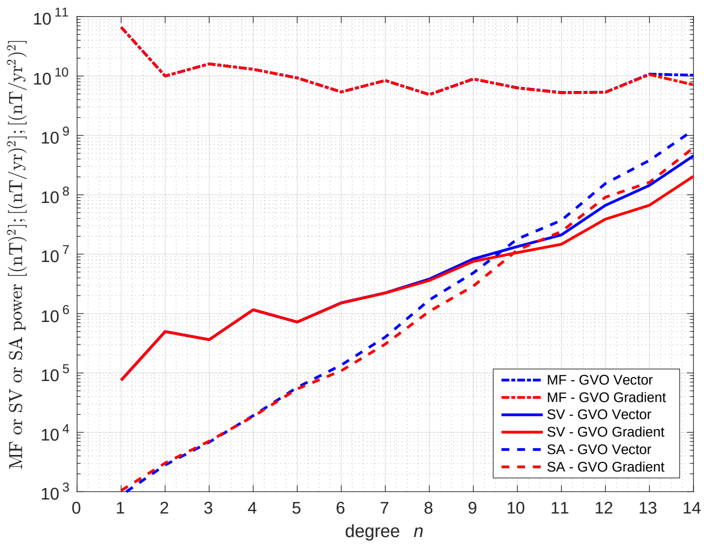

Figure 6. MF (dotted curves), SV (curves) and SA (punctuated curves) CMB mean power spectra of epoch models derived using *Swarm* GVO vector field (blue) and field gradient (red) data truncated at SH degree $n = 14$.

temporal regularization. Spectral curves in blue and red are derived from GVO gradients and GVO vector series, respectively. The SV and SA power spectra derived from GVO gradient tensor series are seen to diverge less rapidly as compared to models derived from GVO vector series, and the SV/SA intersection happens at a slightly higher degree (10 compared to 9). This behaviour is consistent with the analyzes of Kotsiaros & Olsen (2014), who found that gradient observations better constrain SV to higher SH degrees than vector observations. We find (not shown) that we can robustly map the SA at the CMB up to degree 7 using the 4-monthly gradient tensor element data. Although the CMB maps exhibit more noise due to the downward continuation of the field, they display the same distinct SA changes in the Pacific region as those appearing in Figure 5, thus supporting an internal origin of the 2017 SA impulse.

Investigating further these SH models, Figure 7 shows the first time derivative of the internal expansion coefficients, computed based on simple first differences, derived from the GVO vector (blue) and GVO gradient (red) series. Example coefficients are shown for zonal, $m = 0$, terms (top row), tesseral, $m \neq n$, terms (middle row) and sectorial, $m = n$, terms (bottom row). To quantify the scatter level in the epoch coefficient series, standard deviations between the coefficient series and GCV smoothing spline fits (solid curves) are given in each case. Although robust estimation has been employed when deriving these models, outliers can be seen in the both series. A change in the sign of the trend in the SV signal is evident, especially in the sectorial coefficients $\dot{h}_3^3, \dot{h}_4^4, \dot{h}_5^5$, but also in the $\dot{h}_5^3$ coefficient centered on 2017. Figure 8 collects such standard deviations for SH degrees and order up to 12, from models derived using the GVO vector (left plot) and GVO gradient (right plot) series. We generally find less scatter in the GVO gradient series, and especially in the zonal and near-zonal (where m is close to zero) coefficients. For the sectorial terms the scatter levels are low for both series. Use of the vector series results in higher scatter levels for the near-zonal terms for degrees $n > 2$ and orders $m \leq 2$. When also including an external SH expansion for the GVO vector series (middle plot), we are able to reduce the scatter level in the near-zonal coefficients (middle plot of Figure 8), illustrating that using the GVO gradient elements in SH modelling helps in excluding external field signals. Note here that we focus on comparing SH models derived from GVO vector data with those derived solely using GVO gradient data (including an external SH expansion for the GVO gradient series would require vector information as well to obtaining a robust estimation). Global maps (not shown) show that much of the enhanced scatter is related to signals in polar regions being spuriously mapped into the internal field.

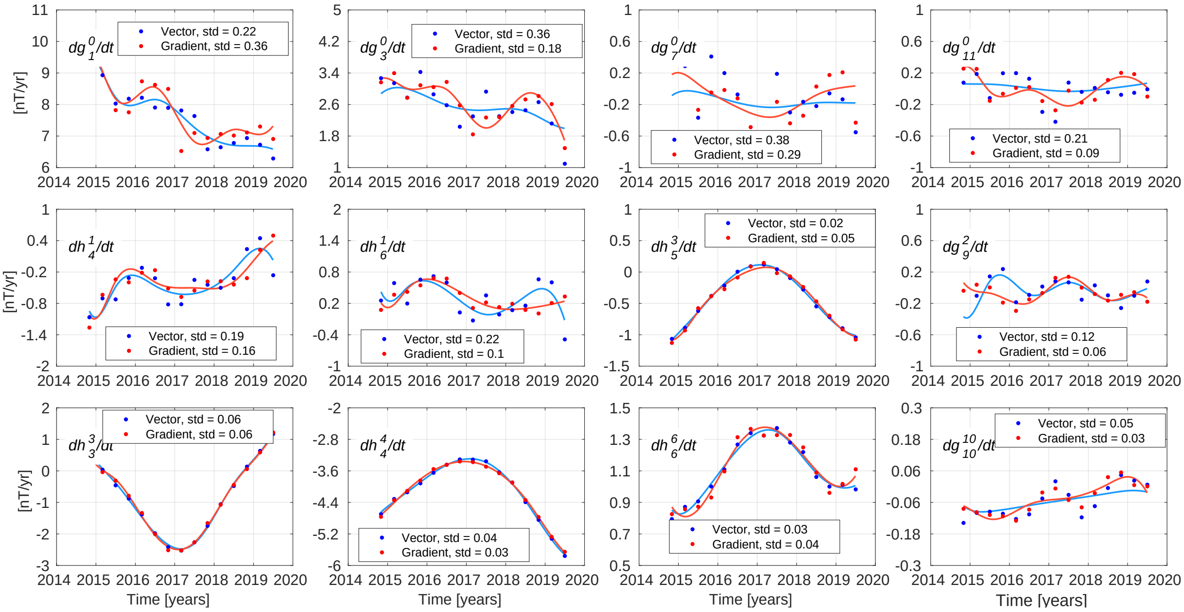

Figure 7. Series of first time derivatives for example internal coefficients dg_n^m/dt and dh_n^m/dt derived from GVO vector (blue dots) and GVO gradient (red dots) data. Standard deviations of differences between the series and a GCV smoothing spline fit (solid curves) to the coefficients are given. Units are nT/yr.

5 DISCUSSION AND CONCLUSIONS

In this study we have extended the existing GVO concept and derived time series of the second-order gradient tensor elements of the geomagnetic field at a global network of 300 locations. We have computed such GVO gradient time series from the mean and differences of vector magnetic field

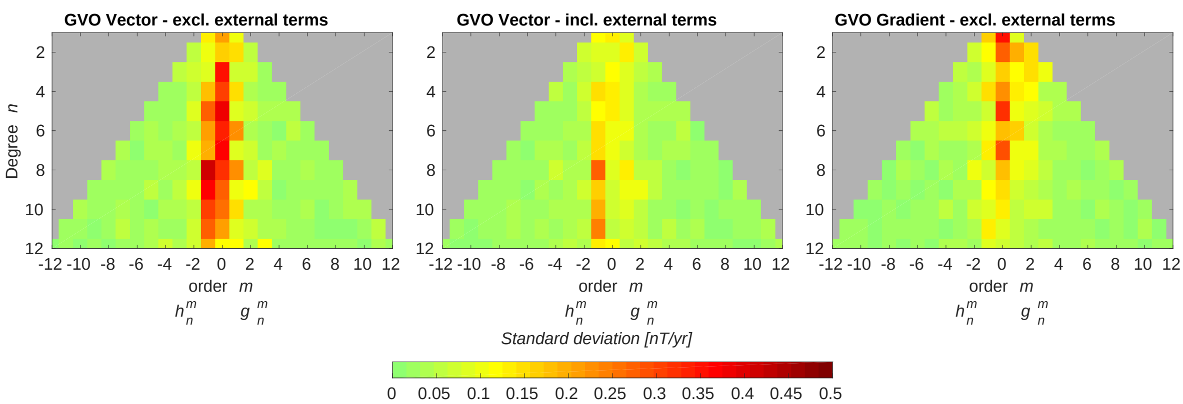

Figure 8. Standard deviations of differences between the first time derivative of internal SH model coefficient series and spline-fitted curves for each series derived from GVO vector data (left plot) and GVO gradient data (right plot), and GVO vector data including an external SH expansion (middle plot). Positive orders m refer to the coefficients dg_n^m/dt, while negative orders refer to dh_n^m/dt coefficients. Units are nT/yr.

measurements, along track and in the east-west direction, from the low Earth orbiting CHAMP and *Swarm* satellites.

The scatter levels for the SV of the gradient tensor elements are higher during CHAMP times than during *Swarm* times. The orbital configuration of the three *Swarm* satellites is clearly advantageous when computing the gradient tensor as more data are available and *Swarm* Bravo, having a slightly higher altitude than Alpha and Charlie, provides more information on the radial gradient and enables better potential determination and superior rms misfit statistics. Higher levels of scatter at polar latitudes are likely due to contaminating fields from polar current systems, while the generally larger misfits during CHAMP times at all latitudes as compared to *Swarm* times, are likely due to less complete data coverage and the closer proximity of the lower flying CHAMP satellite to ionospheric current systems. The SV gradient tensor elements $[\nabla B]_{\theta\theta}$ and $[\nabla B]_{r\theta}$, show lower levels of scatter compared to the other tensor elements, at both polar and at non-polar regions, correctly weighting the various components will be important for future applications.

In order to test for possible improvements in retrieving the SV signal using GVO gradient tensor data alone, we produced simple unregularized SH field models built from the GVO gradient and vector data derived using *Swarm* measurements. Comparing the power spectra of these models supports the findings of Kotsiaros & Olsen (2014), that harmonics of the SV above degree 6 can be better resolved when using gradient tensor data than using vector data. In particular, analysis of the first time derivatives of the SH coefficients, shows that especially zonal and near-zonal harmonics of models derived from GVO gradients have less scatter compared to similar models derived from GVO vector data.

Inspecting SV gradient tensor elements for a GVO located above the Honolulu ground observatory we found evidence in the gradient series for a regional jerk-type event centered on 2017, observed as a characteristic "V" shaped change in the $d\,[\nabla B]_{rr}\,/dt$ and $d\,[\nabla B]_{r\theta}\,/dt$ elements, and as a "Λ" shape in the $d\,[\nabla B]_{\theta\theta}\,/dt$ and $d\,[\nabla B]_{\phi\phi}\,/dt$ elements. In the global GVO SV gradient element records, spanning the years from 2014 to 2020, we find evidence for robust time variations in many of the tensor elements. In particular, intense fluctuations in the Pacific region confined in longitude, suggest a regionally localized geomagnetic impulse event taking place around 2017. This is consistent with ground observatory measurements of the SV of the radial magnetic field component at the Honolulu observatory (e.g. Finlay et al. 2020; Sabaka et al. 2018). By changing the geomagnetic quiet-time and local time selection criteria, we see little change in the amplitude of this jerk signal, supporting the hypothesis that the 2017 event is of internal origin. At the Earth's surface nearby patches of intense change in the SA gradient field, with opposite signs, occurs between 2015.5 and 2018.5. These are found to be limited to latitudes between 25°S to 25°N and to longitudes between 140° to 220°E. In particular, two strong patches of change in the radial gradient of the radial field, with opposite signs, locate the centre of the 2017 jerk event to approximately $0°$N and $170°$E in the central Pacific.

Various geophysical explanations of geomagnetic jerk events, similar to those we have highlighted here in the Pacific region, have been proposed. The possibilities still under discussion include equatorially trapped MAC waves in a possible stratified layer close to the core surface (Buffett & Matsui 2019; Chi-Durán et al. 2020) and equatorial focusing of hydrodynamic waves originating from turbulent convection deep within the core (Aubert & Finlay 2019; Gerick et al. 2021). In that connection the new concept of GVO gradient tensor time series may aid future studies of the appearance and dynamics of geomagnetic jerks, related changes in core flows and core dynamics via e.g. data assimilation.

We have shown that some GVO gradient tensor elements are less affected by correlated errors due to external field unmodelled signals, compared with vector field components. In a follow-up study with Prof. K. Whaler (in prep), we shall present computations and investigations of core surface flows derived from GVO gradient tensor elements series, paying particular attention to the jerk in the Pacific region in 2017.

AVAILABILITY OF DATASETS AND MATERIAL

The GVO gradient tensor data underlying this article and their associated uncertainty estimates are available from `https://data.dtu.dk/`, at (Hammer et al. 2021b). The datasets used in this article are available in the following repositories: Swarm data are available from `https://earth.esa.int/web/guest/swarm/data-access`; CHAMP data are available from `https://isdc.gfz-potsdam.de/champ-isdc`; Ground observatory data are available from `ftp://ftp.nerc-murchison.ac.uk/geomag/Swarm/AUX_OBS/hour/`; The RC-index is available from `http://www.spacecenter.dk/files/magnetic-models/RC/`; The CHAOS-7 model and its updates are available at `http://www.spacecenter.dk/files/magnetic-models/CHAOS-7/`; solar wind speed, interplanetary magnetic field, and Kp-index are available from `https://omniweb.gsfc.nasa.gov/ow.html`.

ACKNOWLEDGMENTS

We thank the GFZ German Research Centre for Geoscience for providing access to the CHAMP MAG-L3 data and the European Space Agency (ESA) for providing access to the *Swarm* L1b data. The high resolution 1-min OMNI data were provided by the Space Physics Data Facility (SPDF), NASA Goddard Space Flight Centre. We thank the staff of the geomagnetic observatories and the INTERMAGNET for providing high-quality observatory data. This project was partly supported by the

European Research Council (ERC) under the European Union's Horizon 2020 research and innovation programme (grant agreement No. 772561). In addition, this study was also partly funded by ESA through the Swarm DISC activities, contract no. 4000109587.

REFERENCES

Aubert, J. & Finlay, C. C., 2019. Geomagnetic jerks and rapid hydromagnetic waves focusing at Earth's core surface, *Nature Geoscience*, **12**(5), 393–398.

Backus, G., Parker, R., & Constable, C., 1996. *Foundations of Geomagnetism*, Cambridge Univ. Press, New York.

Barrois, O., Hammer, M. D., Finlay, C. C., Martin, Y., & Gillet, N., 2018. Assimilation of ground and satellite magnetic measurements: inference of core surface magnetic and velocity field changes, *Geophys. J. Int.*, **215**, 695–712.

Beggan, C. D., Whaler, K. A., & Macmillan, S., 2009. Biased residuals of core flow models from satellite-derived virtual observatories, *Geophys. J. Int.*, **177**(2), 463–475.

Bendat, J. & Piersol, A., 2010. *Random Data, Analysis and Measurement Procedures*, Wiley, New Jersey.

Buffett, B. & Matsui, H., 2019. Equatorially trapped waves in Earth's core, *Geophys. J. Int.*, **218**(2), 1210–1225.

Casotto, S. & Fantino, E., 2009. Gravitational gradients by tensor analysis with application to spherical coordinates, *Journal of Geodesy*, **83**(7), 621–634.

Chi-Durán, R., Avery, M. S., Knezek, N., & Buffett, B. A., 2020. Decomposition of geomagnetic secular acceleration into traveling waves using complex empirical orthogonal functions, *Geophys. Res. Lett.*, p. e2020GL087940.

Constable, C. G., 1988. Parameter estimation in non-Gaussian noise, *Geophys. J. Int.*, **94**(1), 131–142.

Cox, G., Brown, W., Beggan, C., Hammer, M., & Finlay, C., 2020. Denoising Swarm geomagnetic virtual observatories using principal component analysis, doi: 10.5194/egusphere-egu2020-9957.

Domingos, J., Pais, M. A., Jault, D., & Mandea, M., 2019. Temporal resolution of internal magnetic field modes from satellite data, *Earth, Planets and Space*, **71**(1), 1–17.

Finlay, C. C., 2019. Models of the main geomagnetic field based on multi-satellite magnetic data, *Ionospheric Multi-Spacecraft Analysis Tools: Approaches for Deriving Ionospheric Parameters*, **17**, 255.

Finlay, C. C., Kloss, C., Olsen, N., Hammer, M. D., Tøffner-Clausen, L., Grayver, A., & Kuvshinov, A., 2020. The CHAOS-7 geomagnetic field model and observed changes in the South Atlantic Anomaly, *Earth, Planets and Space*, **72**(1), 1–31.

Gerick, F., Jault, D., & Noir, J., 2021. Fast Quasi-Geostrophic Magneto-Coriolis Modes in the Earth's core, *Geophys. Res. Lett.*, **48**(4), e2020GL090803, doi:10.1029/2020GL090803.

Green, P. J. & Silverman, B. W., 1993. *Nonparametric regression and generalized linear models: a roughness penalty approach*, Chapman and Hall.

Hammer, M. D., 2018. *Local Estimation of the Earth's Core Magnetic Field*, Ph.D. thesis, Technical University of Denmark.

Hammer, M. D. & Finlay, C. C., 2019. Local averages of the core–mantle boundary magnetic field from satellite observations, *Geophys. J. Int.*, **216**(3), 1901–1918.

Hammer, M. D., Cox, G., Brown, W., Beggan, C. D., & Finlay, C. C., 2021a. Geomagnetic Virtual Observatories: monitoring geomagnetic secular variation with the Swarm satellites, *Earth, Planets and Space*, **73**(1), 1–22.

Hammer, M. D., Finlay, C. C., & Olsen, N., 2021b. Secular variation signals in magnetic field gradient tensor elements derived from satellite-based geomagnetic virtual observatories., Technical University of Denmark. Dataset. doi:10.11583/DTU.14695590.

Hammer, M. D., Finlay, C. C., & Olsen, N., 2021c. Applications of CryoSat-2 satellite magnetic data in studies of the Earth's core field variations, *Earth, Planets and Space*, **73**(1), 1–22.

Huder, L., Gillet, N., Finlay, C. C., Hammer, M. D., & Tchoungui, H., 2020. COV-OBS.x2: 180 years of geomagnetic field evolution from ground-based and satellite observations, *Earth, Planets and Space*, **72**(1), 1–18.

Kloss, C. & Finlay, C. C., 2019. Time-dependent low latitude core flow and geomagnetic field acceleration pulses, *Geophys. J. Int.*, **217**, 140–168.

Koop, R., 1993. *Global gravity field modelling using satellite gravity gradiometry*, Netherlands Geodetic Comission, Publications on Geodesy, New Series, Number 38, Delft, The Netherlands.

Kotsiaros, S., 2016. Toward more complete magnetic gradiometry with the swarm mission, *Earth, Planets and Space*, **68**(1), 1–13.

Kotsiaros, S. & Olsen, N., 2012. The geomagnetic field gradient tensor, *GEM-International Journal on Geomathematics*, **3**(2), 297–314.

Kotsiaros, S. & Olsen, N., 2014. End-to-end simulation study of a full magnetic gradiometry mission, *Geophys. J. Int.*, **196**(1), 100–110.

Kotsiaros, S., Finlay, C., & Olsen, N., 2015. Use of along-track magnetic field differences in lithospheric field modelling, *Geophys. J. Int.*, **200**(2), 878–887.

Laundal, K. M. & Richmond, A. D., 2017. Magnetic coordinate systems, *Space Science Reviews*, **206**(1-4), 27–59.

Leopardi, P., 2006. A partition of the unit sphere into regions of equal area and small diameter, *Electronic Transactions on Numerical Analysis*, **25**(12), 309–327.

Mandea, M. & Olsen, N., 2006. A new approach to directly determine the secular variation from magnetic satellite observations, *Geophys. Res. Lett.*, **33**(15).

Nogueira, T., Scharnagl, J., Kotsiaros, S., & Schilling, K., 2015. NetSat-4G A four nano-satellite formation for global geomagnetic gradiometry, in *In Proceedings of 10th IAA Symposium on Small Satellites for Earth Observation*.

Olsen, N. & Kotsiaros, S., 2011. Magnetic satellite missions and data, in *Geomagnetic Observations and*

Models, pp. 27–44, Springer.

Olsen, N. & Mandea, M., 2007. Investigation of a secular variation impulse using satellite data: The 2003 geomagnetic jerk, *Earth Planet. Sci. Lett.*, **255**(1), 94–105.

Olsen, N., Lühr, H., Sabaka, T. J., Mandea, M., Rother, M., Tøffner-Clausen, L., & Choi, S., 2006. CHAOS—a model of the Earth's magnetic field derived from CHAMP, Ørsted, and SAC-C magnetic satellite data, *Geophys. J. Int.*, **166**(1), 67–75.

Olsen, N., Lühr, H., Finlay, C. C., Sabaka, T. J., Michaelis, I., Rauberg, J., & Tøffner-Clausen, L., 2014. The CHAOS-4 geomagnetic field model, *Geophys. J. Int.*, **197**(2), 815–827.

Olsen, N., Hulot, G., Lesur, V., Finlay, C. C., Beggan, C., Chulliat, A., Sabaka, T. J., Floberghagen, R., Friis-Christensen, E., Haagmans, R., et al., 2015. The Swarm Initial Field Model for the 2014 geomagnetic field, *Geophys. Res. Lett.*, **42**(4), 1092–1098.

Olsen, N., Ravat, D., Finlay, C. C., & Kother, L. K., 2017. LCS-1: a high-resolution global model of the lithospheric magnetic field derived from CHAMP and Swarm satellite observations, *Geophys. J. Int.*, **211**(3), 1461–1477.

Reed, G., 1973. *Application of kinematical geodesy for determining the shorts wavelength component of the gravity field by satellite gradiometry*, Ph.D. thesis, The Ohio State University, Dept. of Geod Science, Rep. No. 201, Columbus, Ohio.

Riley, K. F., Hobson, M., & Bence, S., 2004. *Mathematical Methods for Physics and Engineering*, Cambridge University Press, Cambridge.

Ritter, P., Lühr, H., Maus, S., & Viljanen, A., 2004. High-latitude ionospheric currents during very quiet times: their characteristics and predictability, in *Annales Geophysicae*, vol. 22, pp. 2001–2014.

Rogers, H. F., Beggan, C. D., & Whaler, K. A., 2019. Investigation of regional variation in core flow models using spherical slepian functions, *Earth, Planets and Space*, **71**(1), 19.

Sabaka, T. J., Hulot, G., & Olsen, N., 2010. Mathematical properties relevant to geomagnetic field modeling, in *Handbook of Geomathematics*, pp. 503–538, Springer.

Sabaka, T. J., Tøffner-Clausen, L., & Olsen, N., 2013. Use of the Comprehensive Inversion method for Swarm satellite data analysis, *Earth, Planets and Space*, **65**(11), 1201–1222.

Sabaka, T. J., Tøffner-Clausen, L., Olsen, N., & Finlay, C. C., 2018. A Comprehensive Model of the Earth's Magnetic Field Determined From 4 Years of Swarm Satellite Observations, *Earth, Planets and Space*, **70**(1), 1–26.

Shore, R. M., 2013. *An improved description of Earth's external magnetic fields and their source regions using satellite data*, Ph.D. thesis, The University of Edinburgh.

Tscherning, C., 1976. Computation of the second-order derivatives of the normal potential based on the representation by a legendre series, *Manuscripta geodaetica*, **1**, 71–92.

APPENDIX A: THE MAGNETIC FIELD GRADIENT TENSOR AND GENERAL COORDINATE TRANSFORMATIONS

Here we provide details on the magnetic gradient tensor and how its elements transform between different coordinate systems. In particular, we are interested in the transformation relations between the tensor components of the local topocentric Cartesian coordinate system described in Section 3.1 and the spherical coordinate system. Formulations from gravimetry of the gravitational gradient tensor (also referred to as the Marussi tensor) can be found in Reed (1973); Koop (1993); Casotto & Fantino (2009); Tscherning (1976). Here we follow the notation of Casotto & Fantino (2009), which is inspired by common usage in general relativity. The reader should however take care concerning the differences between the magnetic and gravity cases, and in particular, of the coordinate systems adopted, i.e. their orientation and whether they are left- or right-handed systems.

Referring to a point P (which would denote a given GVO target point), the usual geocentric system is given by the Cartesian coordinates as $\tilde{x}^p = (\tilde{x}, \tilde{y}, \tilde{z})$ and by the spherical polar coordinates as (r, θ, ϕ), where θ is the colatitude. The geocentric system can be described by the Cartesian unit vectors $(\hat{\mathbf{i}}_\mathbf{1}, \hat{\mathbf{i}}_\mathbf{2}, \hat{\mathbf{i}}_\mathbf{3})$ denoting the basis i_p. At P a local Cartesian coordinate system (z, x, y) is defined by the basis $\mathbf{e}_p$ where $p = 1, 2, 3$, which is same one as used in GVO method, see Section 3.1. This covariant right-handed orthogonal basis is determined by the components of the partial derivatives of the position vector $\mathbf{r}$ as: $\mathbf{e}_1 = \partial\mathbf{r}/\partial r$ pointing radially outwards, $\mathbf{e}_2 = \partial\mathbf{r}/\partial\theta$ pointing to the south and $\mathbf{e}_3 = \partial\mathbf{r}/\partial\phi$ pointing to the east, i.e. similar to the spherical polar basis vector at the target point P. Notice that while the basis vectors i_p are constant in magnitude and direction, the basis vectors e_p have constant magnitude but their directions vary (the same goes for the spherical basis vectors). Thus when computing the spatial derivatives of a vector, the basis vectors also needs to be differentiated as these depend on position. The position vector from origin O to the point P can be written by the geocentric Cartesian coordinates as (Riley et al. 2004)

$$\mathbf{r} = \tilde{x}\hat{\mathbf{i}}_\mathbf{1} + \tilde{y}\hat{\mathbf{i}}_\mathbf{2} + \tilde{z}\hat{\mathbf{i}}_\mathbf{3} = \tilde{x}^p i_p, \tag{A.1}$$

where the summation convention has been used. The Cartesian coordinates are related to the spherical coordinates via (Riley et al. 2004, p. 363)

$$\mathbf{r} = \begin{bmatrix} \tilde{x} \\ \tilde{y} \\ \tilde{z} \end{bmatrix} = r \begin{bmatrix} \sin\theta\cos\phi \\ \sin\theta\sin\phi \\ \cos\theta \end{bmatrix}. \tag{A.2}$$

The magnetic scalar potential, V, can be considered as a tensor of zero-order (or rank). The gradient operator in the generalized coordinates u^p, where $p = 1, 2, 3$, having the covariant basis $\mathbf{e}_p = \partial\mathbf{r}/\partial u^p$

and contravariant basis $\mathbf{e}^p$ can be defined as (Riley et al. 2004; Casotto & Fantino 2009)

$$\nabla = \mathbf{e}^p \frac{\partial}{\partial u^p}. \tag{A.3}$$

Applying the gradient operator to the potential generates a new tensor of one order higher, which is the first-order tensor (vector) describing the magnetic field

$$\nabla V = \frac{1}{h_p} V_p \mathbf{e}^p, \tag{A.4}$$

where we use the notation $V_p = \partial V / \partial u^p$. The metric scale factor h_p is determined by the elements of the metric tensor $g_{pq} = \mathbf{e}_p \cdot \mathbf{e}_q$ (which completely characterize any curvilinear coordinate system) as $h_p = \sqrt{g_{pp}}$. Note that the metric tensor also facilitates the conversion between covariant and contravariant bases (Riley et al. 2004; Casotto & Fantino 2009). Here we follow Casotto & Fantino (2009) and denote the actual elements of the first-order gradient tensor by a semicolon notation

$$V_{;p} = \frac{1}{h_p} V_p \tag{A.5}$$

in order to distinguish them from first order derivatives. Applying the gradient operator to eq.(A.3), produces the second-order gradient operator

$$\begin{aligned} \nabla\nabla &= \mathbf{e}^q \frac{\partial}{\partial u^q}\left(\mathbf{e}^p \frac{\partial}{\partial u^p}\right) \\ &= \mathbf{e}^p \mathbf{e}^q \left(\frac{\partial^2}{\partial u^p \partial u^q} - \Gamma^s_{pq} \frac{\partial}{\partial u^s}\right), \end{aligned} \tag{A.6}$$

where Γ^s_{pq} denotes the Christoffel's symbols of the second kind (an array of numbers describing the derivatives of the covariant basis vector along that same basis), which can be expressed in terms of the metric tensor as (Riley et al. 2004, p. 814)

$$\Gamma^s_{pq} = \frac{1}{2} g^{st} \left(\frac{\partial g_{qt}}{\partial u^p} + \frac{\partial g_{pt}}{\partial u^q} - \frac{\partial g_{pq}}{\partial u^t}\right). \tag{A.7}$$

Applying the operator eq.(A.6) to the magnetic potential V generates the second-order magnetic gradient tensor elements (again adopting the semicolon notation in order to distinguish tensor elements e.g $V_{;rr}$ from the second derivative $V_{rr} = \partial^2 V / \partial r^2$), which can be written using the Christoffel's symbols

$$V_{;pq} = \frac{1}{h_p h_q} \left(\frac{\partial^2 V}{\partial u^p \partial u^q} - \Gamma^s_{pq} \frac{\partial V}{\partial u^s}\right). \tag{A.8}$$

An essential aspect of the first- and second-order tensors is how their elements $V_{;p'}$ or $V_{;p'q'}$ in one coordinate system $u^{p'}$ transforms to a new coordinate system u^p (Casotto & Fantino 2009; Riley et al.

2004, p. 811)

$$V_{;p} = \frac{h_{p'}}{h_p}\frac{\partial u^{p'}}{\partial u^p}V_{;p'} \tag{A.9}$$

$$V_{;pq} = \frac{h_{p'}}{h_p}\frac{h_{q'}}{h_q}\frac{\partial u^{p'}}{\partial u^p}\frac{\partial u^{p'}}{\partial u^q}V_{;p'q'}, \tag{A.10}$$

where the partial derivatives $\partial u^{p'}/\partial u^p$ are expressed by the Jacobian matrix. The Jacobian matrix times the metric scale factor term, can be regarded as a rotation matrix such that we may re-write eqs.(A.9) and (A.10)

$$V_{;p} = V_{;p'}R \tag{A.11}$$

$$V_{;pq} = RV_{;p'q'}R^T, \tag{A.12}$$

having the transformation matrix determined as

$$R = \frac{\partial u^{p'}}{\partial u^p}D, \tag{A.13}$$

where $D = diag(h_{p'}/h_p) = diag(h_{1'}/h_1, h_{2'}/h_2, h_{3'}/h_3)$ is a diagonal 3×3 matrix of the scale factor ratios between the two coordinate systems. Thus equations (A.9) and (A.10) (equivalently eqs.(A.11) and (A.12)) allow us to transform the tensors in one coordinate system, for instance the global $(\tilde{x}, \tilde{y}, \tilde{z})$, to another, for instance (r, θ, ϕ). Let us now consider the two transformations:

a) Transformation from the global Cartesian $(\tilde{x}, \tilde{y}, \tilde{z})$ to the spherical system (r, θ, ϕ)
b) Transformation from the spherical system (r, θ, ϕ) to the local system (x, y, z)

First, we specify the inner products of the basis vectors, the covariant metric tensors for the Cartesian system

$$g_{pg} = \mathbf{e}_p \cdot \mathbf{e}_q = \begin{bmatrix} 1 & 0 & 0 \\ 0 & 1 & 0 \\ 0 & 0 & 1 \end{bmatrix}. \tag{A.14}$$

and the spherical system

$$g_{pg} = \mathbf{e}_p \cdot \mathbf{e}_q = \begin{bmatrix} 1 & 0 & 0 \\ 0 & r^2 & 0 \\ 0 & 0 & r^2\sin^2\theta \end{bmatrix}. \tag{A.15}$$

Thus the metric scale factors of the Cartesian system become

$$h_{\tilde{x}} = 1, \quad h_{\tilde{y}} = 1, \quad h_{\tilde{z}} = 1, \tag{A.16}$$

and for the spherical system

$$h_r = 1, \quad h_\theta = r, \quad h_\phi = r\mathrm{sin}\theta. \tag{A.17}$$

The Christoffel's symbols determined by eq.(A.7) yields 27 values of which 9 are non-zero

$$\Gamma^1_{pq} = \begin{bmatrix} 0 & 0 & 0 \\ 0 & -r & 0 \\ 0 & 0 & -r\mathrm{sin}^2\theta \end{bmatrix}$$
$$\Gamma^2_{pq} = \begin{bmatrix} 0 & \frac{1}{r} & 0 \\ \frac{1}{r} & 0 & 0 \\ 0 & 0 & -\mathrm{cos}\theta\mathrm{sin}\theta \end{bmatrix}$$
$$\Gamma^3_{pq} = \begin{bmatrix} 0 & 0 & \frac{1}{r} \\ 0 & 0 & \frac{\mathrm{cos}\theta}{\mathrm{sin}\theta} \\ \frac{1}{r} & \frac{\mathrm{cos}\theta}{\mathrm{sin}\theta} & 0 \end{bmatrix}. \tag{A.18}$$

Note that for the Cartesian system the Christoffel's symbols are zero as the metric tensor is the identity matrix. In case a) the Jacobian matrix between the spherical coordinates $u^p = (r, \theta, \phi)$ and the Cartesian coordinates $u^{p'} = \tilde{x}^p = (\tilde{x}, \tilde{y}, \tilde{z})$ is

$$\left(\frac{\partial u^{p'}}{\partial u^p}\right) = \frac{\partial(\tilde{x}, \tilde{y}, \tilde{z})}{\partial(r, \theta, \phi)} = \begin{pmatrix} \frac{\partial \tilde{x}}{\partial r} & \frac{\partial \tilde{x}}{\partial \theta} & \frac{\partial \tilde{x}}{\partial \phi} \\ \frac{\partial \tilde{y}}{\partial r} & \frac{\partial \tilde{y}}{\partial \theta} & \frac{\partial \tilde{y}}{\partial \phi} \\ \frac{\partial \tilde{z}}{\partial r} & \frac{\partial \tilde{z}}{\partial \theta} & \frac{\partial \tilde{z}}{\partial \phi} \end{pmatrix} = \begin{pmatrix} \mathrm{sin}\theta\mathrm{cos}\phi & r\mathrm{cos}\theta\mathrm{cos}\phi & -r\mathrm{sin}\theta\mathrm{sin}\phi \\ \mathrm{sin}\theta\mathrm{sin}\phi & r\mathrm{cos}\theta\mathrm{sin}\phi & r\mathrm{sin}\theta\mathrm{cos}\phi \\ \mathrm{cos}\theta & -r\mathrm{sin}\theta & 0 \end{pmatrix}, \tag{A.19}$$

while in case b) the Jacobian matrix between the local Cartesian coordinates $u^p = (z, x, y)$ and the spherical coordinates $u^{p'} = (r, \theta, \phi)$ is

$$\left(\frac{\partial u^{p'}}{\partial u^p}\right) = \frac{\partial(r, \theta, \phi)}{\partial(z, x, y)} = \begin{pmatrix} \frac{\partial r}{\partial z} & \frac{\partial r}{\partial x} & \frac{\partial r}{\partial y} \\ \frac{\partial \theta}{\partial z} & \frac{\partial \theta}{\partial x} & \frac{\partial \theta}{\partial y} \\ \frac{\partial \phi}{\partial z} & \frac{\partial \phi}{\partial x} & \frac{\partial \phi}{\partial y} \end{pmatrix} = \begin{pmatrix} 1 & 0 & 0 \\ 0 & 1 & 0 \\ 0 & 0 & 1 \end{pmatrix}. \tag{A.20}$$

Considering case a), we use eqs.(A.11) and (A.12) to obtain the relations written here in matrix form

$$\frac{\partial V}{\partial(r, \theta, \phi)} = \frac{\partial V}{\partial(\tilde{x}, \tilde{y}, \tilde{z})} R \tag{A.21}$$
$$\frac{\partial^2 V}{\partial(r, \theta, \phi)^2} = R \frac{\partial V}{\partial(\tilde{x}, \tilde{y}, \tilde{z})^2} R^T, \tag{A.22}$$

where R is determined by eq.(A.13) using eqs.(A.16), (A.17) and (A.19).

Likewise considering case b), we use the relations eqs.(A.11) and (A.12) written here in matrix form

$$\frac{\partial V}{\partial(z,x,y)} = \frac{\partial V}{\partial(r,\theta,\phi)} R \tag{A.23}$$

$$\frac{\partial^2 V}{\partial(z,x,y)^2} = R \frac{\partial V}{\partial(r,\theta,\phi)^2} R^T, \tag{A.24}$$

where R is determined by eq.(A.13) using eqs.(A.16), (A.17) and (A.20). Here the first-order tensor (i.e. the magnetic field vector) in the spherical polar coordinates is given by eq.(A.4) using the metric scale factors eq.(A.17)

$$\nabla V = V_r \hat{\mathbf{e}}_{\mathbf{r}} + \frac{1}{r} V_\theta \hat{\mathbf{e}}_\theta + \frac{1}{r\mathrm{sin}\theta} V_\phi \hat{\mathbf{e}}_\phi, \tag{A.25}$$

such that the first-order magnetic tensor elements in the local Cartesian system by eq.(A.23) are given by the relations

$$V_{;z} = V_r, \quad V_{;x} = \frac{1}{r} V_\theta, \quad V_{;y} = \frac{1}{r\mathrm{sin}\theta} V_\phi. \tag{A.26}$$

The second-order tensor in the spherical polar coordinates is given by eq.(A.8) using the Christoffel's symbols from eq.(A.18) and metric scale factors eq.(A.17)

$$\begin{aligned}
\nabla\nabla V = {} & V_{rr} \hat{\mathbf{e}}_{\mathbf{r}} \hat{\mathbf{e}}_{\mathbf{r}} + \left(\frac{1}{r} V_{\theta r} - \frac{1}{r^2} V_\theta \right) \hat{\mathbf{e}}_{\mathbf{r}} \hat{\mathbf{e}}_\theta + \left(\frac{1}{r\mathrm{sin}\theta} V_{\phi r} - \frac{1}{r^2\mathrm{sin}\theta} V_\phi \right) \hat{\mathbf{e}}_{\mathbf{r}} \hat{\mathbf{e}}_\phi \\
& + \left(\frac{1}{r} V_{r\theta} - \frac{1}{r^2} V_\theta \right) \hat{\mathbf{e}}_\theta \hat{\mathbf{e}}_{\mathbf{r}} + \left(\frac{1}{r^2} V_{\theta\theta} - \frac{1}{r} V_r \right) \hat{\mathbf{e}}_\theta \hat{\mathbf{e}}_\theta + \left(\frac{1}{r^2\mathrm{sin}\theta} V_{\phi\theta} - \frac{\mathrm{cos}\theta}{r^2\mathrm{sin}^2\theta} V_\phi \right) \hat{\mathbf{e}}_\theta \hat{\mathbf{e}}_\phi \\
& + \left(\frac{1}{r\mathrm{sin}\theta} V_{r\phi} - \frac{1}{r^2\mathrm{sin}\theta} V_\phi \right) \hat{\mathbf{e}}_\phi \hat{\mathbf{e}}_{\mathbf{r}} + \left(\frac{1}{r^2\mathrm{sin}\theta} V_{\theta\phi} - \frac{\mathrm{cos}\theta}{r^2\mathrm{sin}^2\theta} V_\phi \right) \hat{\mathbf{e}}_\phi \hat{\mathbf{e}}_\theta + \cdots \\
& + \left(\frac{1}{r^2\mathrm{sin}^2\theta} V_{\phi\phi} + \frac{1}{r} V_r + \frac{\mathrm{cos}\theta}{r^2\mathrm{sin}\theta} V_\theta \right) \hat{\mathbf{e}}_\phi \hat{\mathbf{e}}_\phi.
\end{aligned} \tag{A.27}$$

Note here the convention of notation $V_{rr} = \partial^2 V / \partial r^2$ and $V_{\theta r} = \partial^2 V / \partial\theta\partial r$ which is different from the tensor element notation i.e. $V_{;rr}$ and $V_{;\theta r}$. This means that the relations between the gradient tensor elements in the local Cartesian system and the gradient tensor described in the spherical system are given by eq.(A.24)

$$
\begin{aligned}
V_{;zz} &= V_{rr} \\
V_{;xz} &= \frac{1}{r}V_{\theta r} - \frac{1}{r^2}V_\theta \\
V_{;yz} &= \frac{1}{r\mathrm{sin}\theta}V_{\phi r} - \frac{1}{r^2\mathrm{sin}^2\theta}V_\phi \\
V_{;zx} &= \frac{1}{r}V_{r\theta} - \frac{1}{r^2}V_\theta \\
V_{;xx} &= \frac{1}{r^2}V_{\theta\theta} + \frac{1}{r}V_r \\
V_{;yx} &= \frac{1}{r^2\mathrm{sin}^2\theta}V_{\phi\theta} - \frac{\mathrm{cos}\theta}{r^2\mathrm{sin}^2\theta}V_\phi \\
V_{;zy} &= \frac{1}{r\mathrm{sin}\theta}V_{r\phi} - \frac{1}{r^2\mathrm{sin}\theta}V_\phi \\
V_{;xy} &= \frac{1}{r^2\mathrm{sin}\theta}V_{\theta\phi} - \frac{\mathrm{cos}\theta}{r^2\mathrm{sin}^2\theta}V_\phi \\
V_{;yy} &= \frac{1}{r^2\mathrm{sin}^2\theta}V_{\phi\phi} + \frac{1}{r}V_r + \frac{\mathrm{cos}\theta}{r^2\mathrm{sin}\theta}V_\theta.
\end{aligned}
\tag{A.28}
$$

At the position P (being the GVO target point), we therefore have the following identifications between the tensor elements in the local Cartesian and the spherical systems

$$V_{;zz} = V_{;rr} \quad V_{;zx} = V_{;r\theta} \quad V_{;zy} = V_{;r\phi} \tag{A.29}$$

$$V_{;xz} = V_{;\theta r} \quad V_{;xx} = V_{;\theta\theta} \quad V_{;xy} = V_{;\theta\phi} \tag{A.30}$$

$$V_{;yz} = V_{;\phi r} \quad V_{;yx} = V_{;\phi\theta} \quad V_{;yy} = V_{;\phi\phi}. \tag{A.31}$$

In order to express the gradient tensor in Cartesian coordinates, we note that the metric tensor becomes the identity matrix meaning that the metric scale factors h_p becomes unity, and all of the Christoffel's symbols becomes zero such that the gradient tensor is given by eq.(A.8)

$$
\nabla\mathbf{B} = -\begin{pmatrix} \frac{\partial^2 V}{\partial z^2} & \frac{\partial^2 V}{\partial x\partial z} & \frac{\partial^2 V}{\partial y\partial z} \\ \frac{\partial^2 V}{\partial z\partial x} & \frac{\partial^2 V}{\partial x^2} & \frac{\partial^2 V}{\partial y\partial x} \\ \frac{\partial^2 V}{\partial z\partial y} & \frac{\partial^2 V}{\partial x\partial y} & \frac{\partial^2 V}{\partial y^2} \end{pmatrix} = -\begin{pmatrix} V_{;zz} & V_{;zx} & V_{;zy} \\ V_{;xz} & V_{;xx} & V_{;xy} \\ V_{;yz} & V_{;yx} & V_{;yy} \end{pmatrix} = \begin{pmatrix} [\nabla B]_{zz} & [\nabla B]_{zx} & [\nabla B]_{zy} \\ [\nabla B]_{xz} & [\nabla B]_{xx} & [\nabla B]_{xy} \\ [\nabla B]_{yz} & [\nabla B]_{yx} & [\nabla B]_{yy} \end{pmatrix},
\tag{A.32}
$$

where the minus sign comes from defining the field as the negative gradient of the potential. We recall that the semicolon notation denotes tensor elements following Casotto & Fantino (2009), and not the second order spatial derivatives. However, in the case of the gradient tensor in Cartesian coordinates, these two are equivalent cf. eq.(A.32).

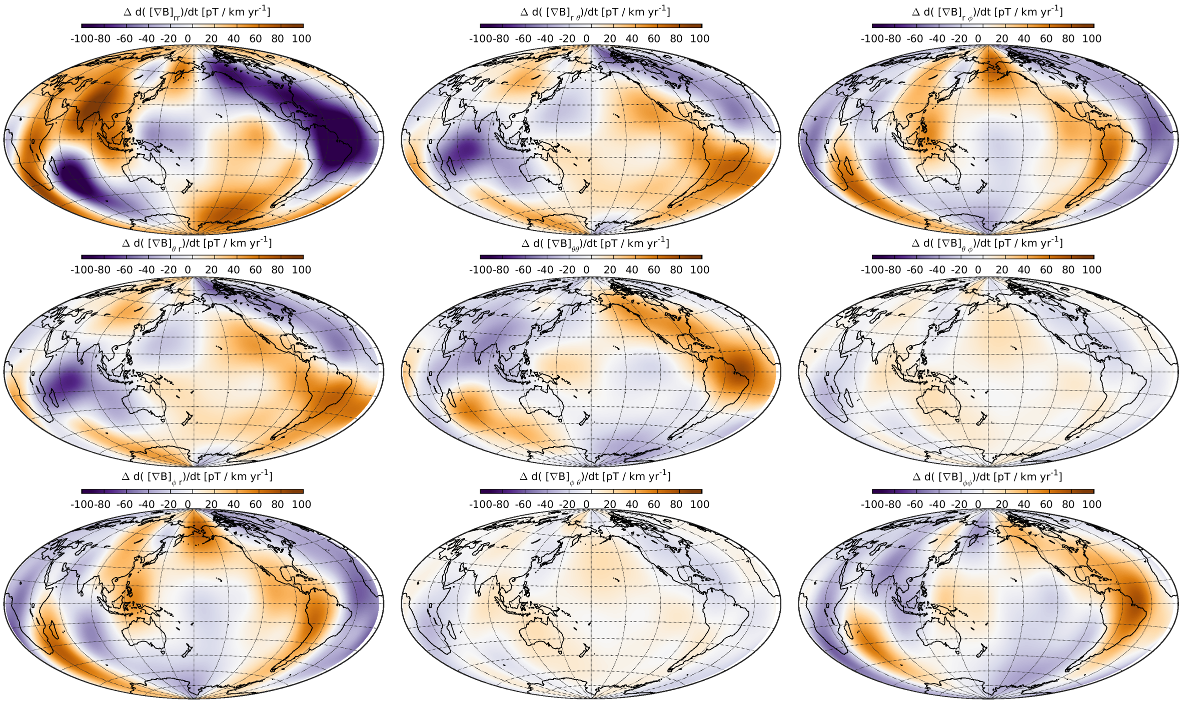

[H]

Figure A1. All terms of the SV gradient tensor at the Earth's surface in 2018.0, CHAOS-7 for $n \leq 16$.

APPENDIX B: SV FIELD GRADIENT TENSOR

Using the CHAOS-7 model for degrees $n \leq 16$ (Finlay et al. 2020), predictions of the SV gradient tensor elements at the Earth's surface in 2018.0 are shown in Figure A1. Figure A2 presents the "gradient term" elements of the SV gradient tensor while Figure A3 presents the "field term" elements of the SV gradient tensor. Here it should be noted that the trace of the tensor is only zero when considering the complete gradient tensor (Figure A1), and not when look at the "field derivative term" (Figure A2) and "field term" (Figure A3) parts.

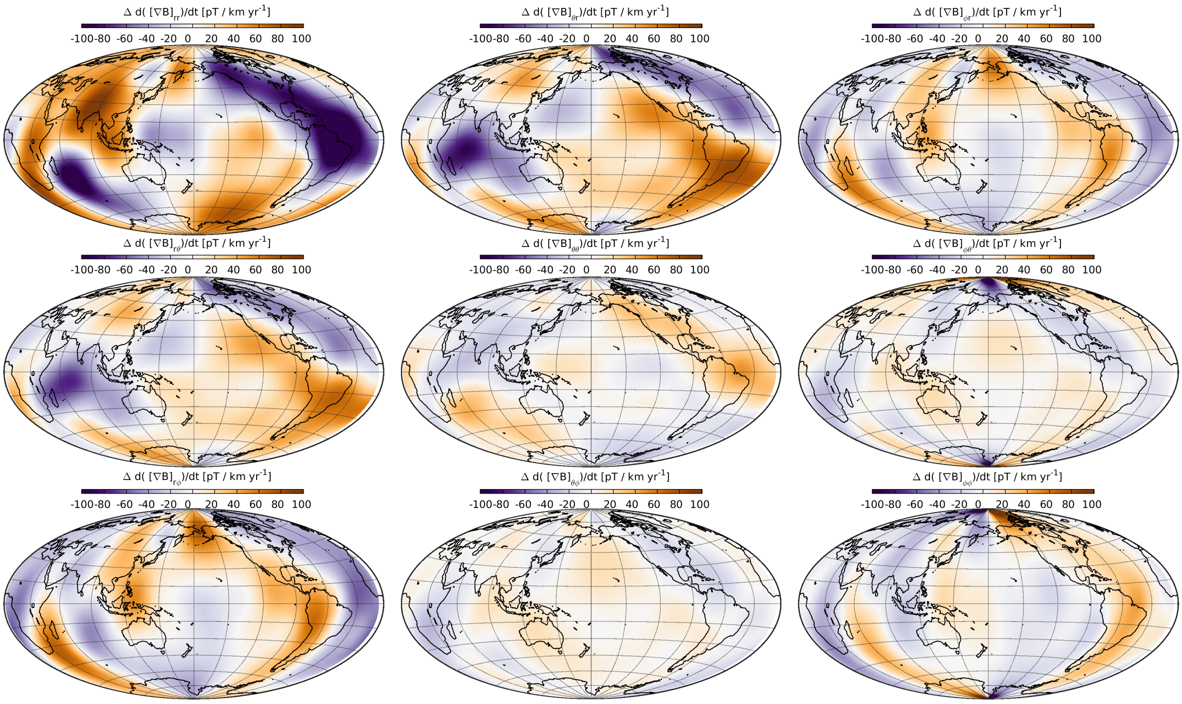

[H]

Figure A2. First terms of the SV gradient tensor at the Earth's surface in 2018.0, CHAOS-7 for $n \leq 16$.

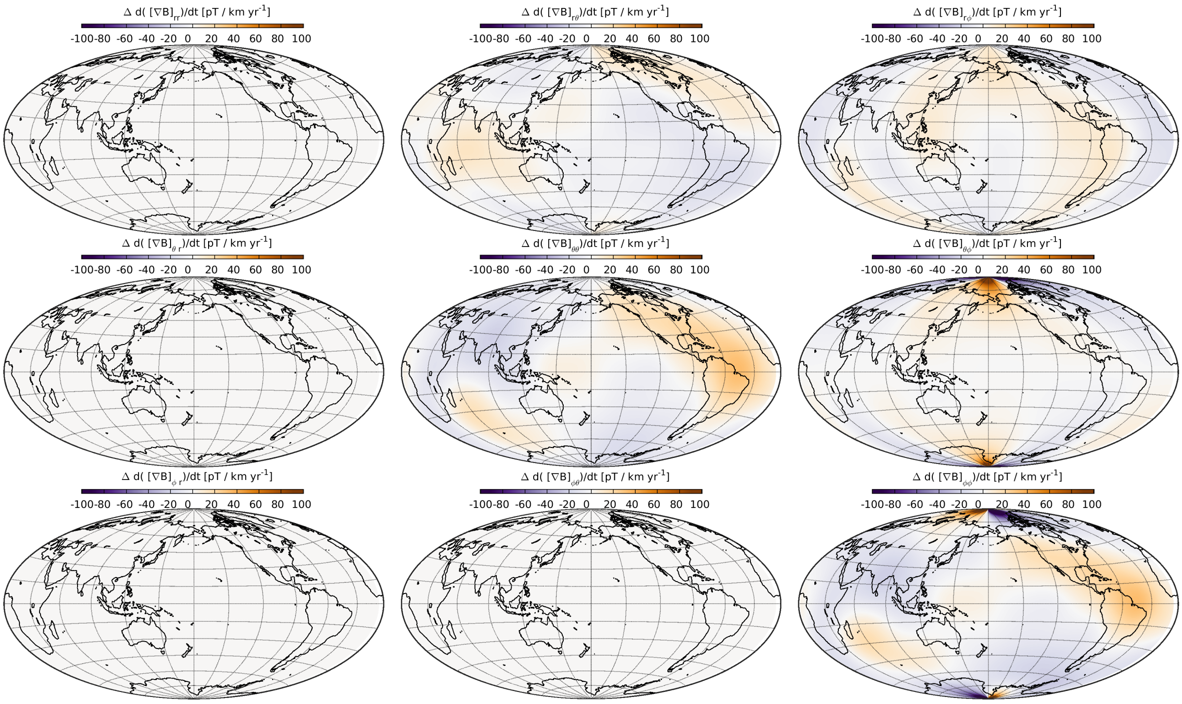

[H]

Figure A3. Second terms of the SV gradient tensor at the Earth's surface in 2018.0, CHAOS-7 for $n \leq 16$.